University of Southern Queensland

Faculty of Health, Engineering & Sciences

Resonator Probe for Photoacoustic Measurement

A dissertation submitted by

David McLaughlin

in fulfilment of the requirements of

ENG4112 Research Project

towards the degree of

Bachelor of Electrical and Electronic Engineering

Submitted: October, 2014

Abstract

Despite major technological advances in photoacoustic spectroscopy over the past four decades, a widely-applicable solution to compensating for ambient temperature sensitivity has not been documented. Temperature changes cause the resonant frequency of the cell to drift, resulting in a suboptimal signal. If the resonant frequency of a photoacoustic cell is detectable in real time, the laser frequency can be modulated to match the adjusted frequency.

To detect and track the change in resonant frequency of a photoacoustic cell in real time, a generalised algorithm is developed using a computer soundcard and MATLAB software.

The relationship between resonator dimensions, temperature, and the speed of sound is described for the case of an open-cell resonator, and the process of developing a software model with constraints imposed by prototype construction limitations is discussed. Following initial positive results from simulations, the physical resonator cell is constructed to validate the theoretical results against measured values.

Initial results indicating that the performance of the prototype was poorer than anticipated by simulations were attributed to distortions introduced by windowing frames for FFT processing. A novel method of pre-processing windowed frames of an audio signal to rectify this problem is detailed, and the speed and accuracy of the developed frequency detection algorithm under varying conditions is analysed.

Although the algorithm developed is shown to track frequency changes with a high degree of accuracy, the technique adopted to determine changes in resonant frequency of a photoacoustic cell is ultimately found to be unsuccessful.

University of Southern Queensland

Faculty of Health, Engineering & Sciences

ENG4111/2 *Research Project*

Limitations of Use

Certification of Dissertation

I certify that the ideas, designs and experimental work, results, analyses and conclusions set out in this dissertation are entirely my own effort, except where otherwise indicated and acknowledged.

I further certify that the work is original and has not been previously submitted for assessment in any other course or institution, except where specifically stated.

David McLaughlin

0050086017

Signature

Date

Acknowledgments

First and foremost, I must acknowledge the deep debt of gratitude I owe to my thesis supervisor, Dr. John Leis, for his advice and support over the past twelve months. From the genesis of the idea, development of the research focus, and through to completion, Dr. Leis has always been available when I have need technical assistance, moral support, or a much-needed reminder that demonstrable progress was required. He has replied to my enquiries at hours that lesser men believe only occur once in a day, and encouraged me to persevere when the more prudent among us would have struck a match to the bonfire of abandonment. In short, this document is a testament to the ability of an exceptional mentor to maximise the achievement of an unremarkable student, and I am grateful to have been the recipient of such dedication.

I deeply appreciate the contributions and sacrifices my family has made throughout the production of my thesis: my wife, for keeping me fed, watered, and sane; my daughter, for breaking the drudgery of writing with extended shopping trips; my elder son, for his earnest advice and confident assertions that I am wrong, regardless of all evidence to the contrary; and my younger son, for listening patiently to my travails long past any measure of reasonableness. You are my world, and I love you all.

David McLaughlin

University of Southern Queensland

October 2014

Contents

Abstract **i**

Acknowledgments **iv**

List of Figures **vii**

List of Tables **x**

Chapter 1 Introduction **1**

1.1 History of Photoacoustic Spectroscopy 2

1.2 Photoacoustic Spectroscopy in a Gaseous Medium 3

1.2.1 Modulation of the Light Source 4

1.2.2 Selectivity 5

1.2.3 Resonant Cells 5

1.3 Literature Review 7

1.4 Research Focus 11

Chapter 2 Resonant Frequency Tracking Algorithm **12**

2.1 Effect of Temperature on Resonant Frequency 13

2.2 Algorithm Development and Resonator Simulation 17

2.2.1 Model Constraints 17

2.2.2 Base Frequency FFT 21

2.2.3 Variable Frequency FFT 23

Chapter 3 Resonator Prototype **28**

3.1 Materials and Construction 29

3.2 Frequency Response Curve 31

3.3 Fixed Sine Wave Response with Resonator 35

3.4 Chirp Response with Resonator 36

3.5 Frequency Tracking Response with Resonator 38

3.6 Measuring Cell Resonant Frequency 45

Chapter 4 Conclusion and Further Work **48**

References **52**

Appendix A Project Specification **58**

Appendix B Job Safety Analysis Forms **60**

Appendix C Source Code **68**

Appendix D Manufacturer Data Sheets **79**

List of Figures

1.1 Basic arrangement of a photoacoustic measuring device 1

1.2 Relative frequency of occurrence of terms 'CO_2 laser' and 'photoacoustic', 1950-2008 3

1.3 Steps in photoacoustic spectroscopy 4

1.4 Multivariate gas analysis 5

1.5 Common resonant photoacoustic cells 6

1.6 Modulated laser CHIRP, resultant acoustic waveform, and processed signal 9

1.7 Corrected response of applied square wave 10

1.8 Time and frequency domain plots of superimposed sine waves 10

2.1 Simple acoustic resonator constructed from a straight length of pipe . . 13

2.2 Simplified Helmholtz acoustic resonator arrangement 14

2.3 Change in speed of sound with varying molecular weight at 25 °C 15

2.4 Change in speed of sound and resonant frequency shift with temperature change 17

2.5 Simulated pure 1600 Hz sine wave sampled at 44.1 kHz 21

2.6 FFT of pure 1600 Hz sine wave sampled at 44.1 kHz 21

2.7 Simulated 1600 Hz sine wave with noise sampled at 44.1 kHz 22

2.8 FFT of 1600 Hz sine wave with noise sampled at 44.1 kHz 22

2.9 FFT of 1600 Hz to 1630 Hz chirp signal 23

2.10 Example of FFT window application 24

2.11 Frequency tracking chart using a Hamming window of 4410 samples and 10% window overlap 25

2.12 Frequency tracking with different size Hamming windows 25

2.13 Three-segment frequency tracking charts with Hamming windows 26

2.14 Three-segment frequency tracking chart using a rectangular window of 6300 samples and no overlap 27

3.1 Replacing laser with speaker in resonator assembly 28

3.2 Dimensional drawing of resonator prototype 30

3.3 Fully assembled prototype resonator used for testing) 31

3.4 500 Hz to 2500 Hz bandpass filter used for initial testing 32

3.5 Initial microphone and speaker frequency response curve without resonator 33

3.6 Computer audio manager application - noise suppression and echo cancelling on microphone 34

3.7 Combined microphone and speaker frequency response curve without resonator 35

3.8 FFT of 1600 Hz audio wave from resonator 36

3.9 Magnified section of 1600 Hz resonator FFT, 1590 Hz to 1610 Hz 37

3.10 Combined microphone and speaker frequency response curve with resonator 38

3.11 Frequency response curves with microphone in and out of resonator . . 39

3.12 Frequency change tracking with window size of 8820 samples 40

3.13 Window overlap shapes 40

3.14 Hann window with 11025 samples and overlap of 1060 and 1070 samples 41

3.15 Frequency tracking algorithm - most accurate results with original algorithm 42

3.16 Modified frequency tracking algorithm - three segments, partial waveforms discarded 44

3.17 Modified frequency tracking algorithm - five segments, partial waveforms discarded 44

3.18 Resonant frequency tracking with 40 Hz window and 5 Hz steps 46

3.19 FFT of 20 Hz window with 2 Hz steps showing separation between frequencies 46

3.20 FFT of 20 Hz window with 0.05 Hz steps showing unequal energy distribution across frequencies 47

List of Tables

2.1 Photoacoustic cell resonant frequency sensitivity to temperature variations 16

3.1 Speed and accuracy of different windows styles, frame sizes, and frame overlaps 42

Chapter 1

Introduction

If a solid, liquid, or gaseous sample is impinged upon by a beam of light, the sample absorbs energy from the light, causing heating in the immediate area of the absorbed light. A pressure wave expands out from the heated area, creating a faint, but perceptible, noise. If the beam of light striking the sample is periodic, sample heating and the subsequent noise produced will occur with a frequency equal to the frequency of the beam of light (Koskinen, Fonsen, Kauppinen & Kauppinen 2006). This phenomenon is known as the *photoacoustic effect*. Photoacoustic spectroscopy is the quantitative analysis of the sound produced by the photoacoustic effect to determine the proportion of a component of the sample. An example of a basic device used to make these measurements is reproduced in Figure 1.1.

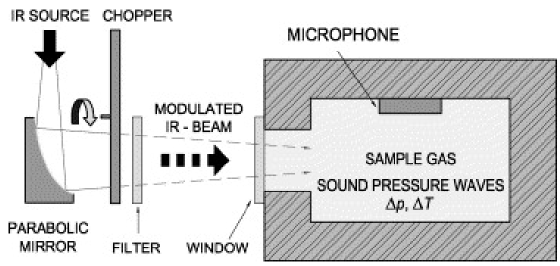

Figure 1.1: Basic arrangement of a photoacoustic measuring device (Koskinen et al. 2006)

Techniques for photoacoustic spectroscopy have been constantly refined from the 1970s onward. As noted in Besson, Schilt & Thévenaz (2006), photoacoustic spectrometry has found widespread application in industry due to the excellent sensitivity, selectivity, and linearity of the results, and the versatility of the equipment. It has been used for the detection of cancer biomarkers in blood samples (Dickherber 2008, Mallidi, Larson, Tam, Joshi, Karpiouk, Sokolov & Emelianov 2009), ammonia leak detection (Timmer, Olthuis & Berg 2005), NO_2 pollution measurements along roadways (Meyer & Sigrist 1990), and electroplating thicknessing (Berg, VanderNoot, Barradas & Lai 1994).

In spite of the enthusiastic and widespread adoption of photoacoustic spectroscopy, there are a few shortcomings with the technique. Chief amongst the problems are the sensitivity of the measuring apparatus to changes in the temperature, pressure, or composition of carrier (buffer) gases of the sample being measured (Szakáll, Varga, Pogány, Bozóki & Szabó 2009, Borowski & Starecki 2008). High-Q (high amplification) resonant photoacoustic cells are especially susceptible to this flaw, exhibiting a change in resonant frequency of about 1% for each 0.6 °C change in sample temperature (Miklós, Hess & Bozóki 2001). There have been attempts to alleviate this problem by scanning the modulation frequencies (Szakáll et al. 2009), real-time calculation of resonant frequency based on measured temperature, and through active resonance tracking with an acoustic oscillator (Angeli, Bozóki, Miklós, Lörincz, Thöny & Sigrist 1991). However, these approaches involve additional expense or slow determination of the resonant frequency, neither of which is desirable. The alternative, controlling the pressure and temperature of the sample, reduces the simplicity of the sample handling system and increases the cost and complexity of the device.

In this report, existing methods of identifying and tracking the resonant frequency of photoacoustic cells under varying ambient conditions are reviewed. The intent of the literature review is to gain an understanding of how the techniques that are currently applied can be be extended or modified in order to achieve similar results more simply and rapidly.

1.1 History of Photoacoustic Spectroscopy

The photoacoustic effect was first described by Alexander Graham Bell in 1880, arising from his experiments with sound transmission over long distances (Bell 1880). He found that a focused, pulsing beam of sunlight striking a thinly-cut selenium sample produced an audible signal, with the amplitude of the signal being greatest when the frequency of the light beam was at the fundamental frequency of the resonator in which the sample was placed. Bell theorised that the sound was caused by the expansion and contraction of the sample as it absorbed the light at a high frequency.

Due to the primitive technology available for analysis of the acoustic signal, development of photoacoustic spectroscopy lay dormant for more than five decades following Bell's initial experiments. In 1938, Viengerov (cited in Bialkowski (1996)) briefly resurrected the subject when he used photoacoustic spectroscopy to produce a quantitative analysis of gas concentration in a sample. However, serious analysis of the photoacoustic effect did not begin in earnest until the development of laser technology in the late 1960s. Figure 1.2 illustrates the surge of interest in the field paralleling the introduction of commercially-available lasers. The introduction of a coherent, high-powered light source into photoacoustic experiments in the form of CO and CO_2 lasers corresponded with rapid improvements in the quality of the resultant signals. Reports of the first parts-per-billion measurements achieved with photoacoustic spectroscopy followed soon after (Kreuzer 1971). Rapid advancements in tunable laser technology and detection equipment now make it possible to detect concentrations of some gases down to a level of parts per trillion (Kalkman & van Kesteren 2008, Spagnolo, Patimisco, Borri, Scamarcio, Bernacki & Kriesel 2013).

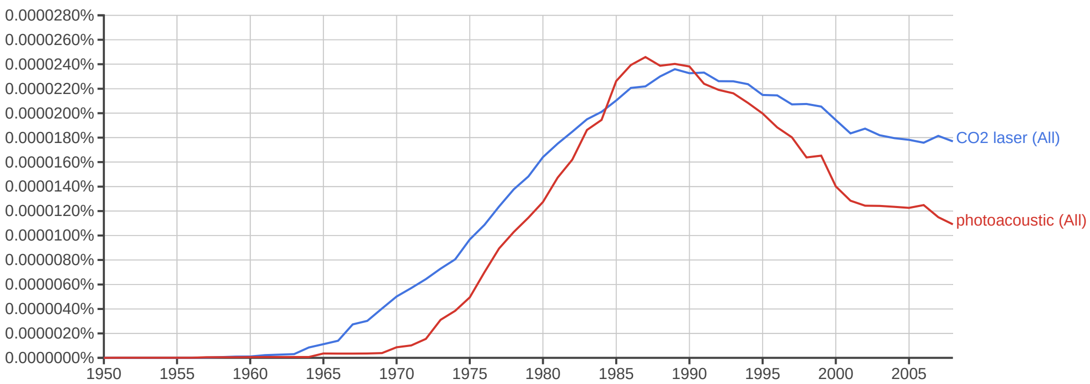

Figure 1.2: Relative frequency of occurrence of terms 'CO_2 laser' and 'photoacoustic', 1950-2008 (Google 2013)

1.2 Photoacoustic Spectroscopy in a Gaseous Medium

Production and detection of the photoacoustic effect in gases is functionally identical to that in solids. As illustrated in Figure 1.3, Miklós et al. (2001) and Elia, Lugarà, Di Franco & Spagnolo (2009) describe the same basic steps in photoacoustic spectroscopy generation and detection in gases:

1. Absorption of modulated light by molecules in the sample and localised release of heat in the gas sample due to relaxation of the excited states (i.e. molecular collisions)

2. Generation of a periodic pressure wave at the modulation frequency.

3. Detection of the pressure wave as an acoustic signal using a microphone, tuning fork, or another frequency detection mechanism.

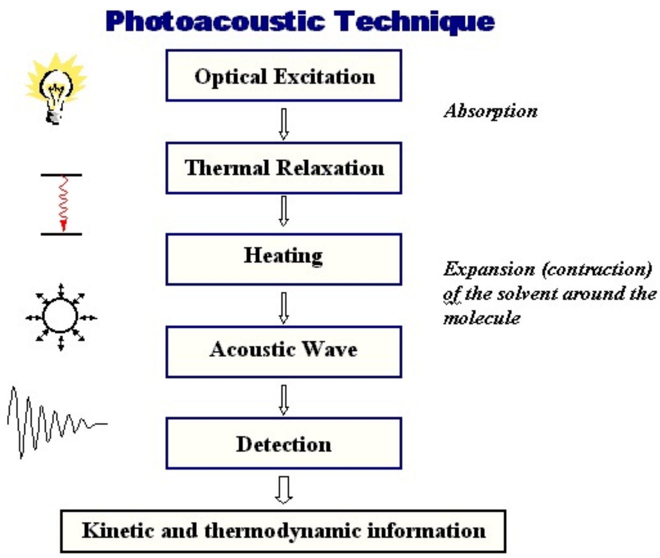

Figure 1.3: Steps in photoacoustic spectroscopy (Leytner & Hupp 2000)

1.2.1 Modulation of the Light Source

Modulation of the light source can be accomplished through the use of a chopper motor (a spinning, perforated disk periodically interrupting the light source), or, preferably, by the use of a pulsed laser. As explained in Tam (1986), the pulsed laser can be operated at high power for very short periods of time, resulting in a correspondingly large acoustic signal. In contrast, a continuous wave laser operates at a duty cycle of up to 50% and consequently operates at lower power output and therefore results in a comparatively small acoustic signal. In either case, the acoustic signal generated through the photoacoustic effect is of a very small absolute magnitude, and can be modified by increasing or decreasing the power delivered by the laser. As the frequency of the generated acoustic wave is equal to the frequency of the modulated light, the modulation frequency must be within the audible range of approximately 100 Hz to 5 kHz in order to fall within the flat frequency response of a typical piezoelectric or electret microphone.

1.2.2 Selectivity

In multivariate gas samples, the components of interest can be targeted by filtering the light source such that only wavelengths strongly absorbed by the required component are admitted into the photoacoustic cell. Alternatively, the laser illuminating the sample can be tuned to supply light of an appropriate wavelength, or to be tuned through a sequence of wavelengths which target each component in turn. Figure 1.4 demonstrates the multiple spectra achievable by a laser able to be tuned between 1015 cm^{-1} and 1240 cm^{-1}. Control of the light wavelength provides the selectivity which is one of the hallmarks of photoacoustic spectroscopy.

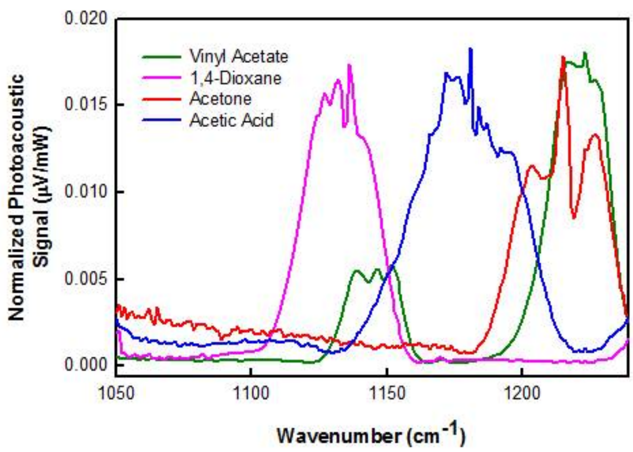

Figure 1.4: Multivariate gas analysis (Holthoff et al. 2010)

1.2.3 Resonant Cells

Although the photoacoustic effect is detectable in open channels (Bonno, Laporte & D'Leon 2005), the effect is more pronounced if the cell is closed or sealed. Cells with a smaller volume result in acoustic signals of greater magnitude, as a higher proportion of the cell volume is heated by the light source to create the acoustic signal. However, even with small photoacoustic cell volumes and high laser power, the acoustic signal still requires amplification in order to be detected. Electrical amplification results in a fairly poor signal to noise ratio (SNR), as the noise floor and acoustic signal are of the same order of magnitude (Mattiello 2008). Exacerbating the problem further, the SNR worsens as the cell volume and modulation frequency decrease (Miklós et al. 2001).

The modern solution to this problem is the same as that employed by Alexander Graham Bell: construct a photoacoustic cell that has a resonant frequency equal to the frequency of the modulated light source. Resonant cells boost the signal through constructive interference at the frequency where standing waves are created inside the cell; depending on the frequency and size of the cell, multiple harmonics of a signal may be present.

The quality factor, or Q factor, of a cell characterises the bandwidth of a resonant cell relative to its centre frequency. As the bandwidth narrows, the Q factor increases. However, high-Q cells, with a Q factor exceeding 50 (Miklós et al. 2001), are sensitive to changes in temperature; a small change in frequency moves the signal a relatively large distance from the resonator's centre frequency. Conversely, low-Q cells are impacted more heavily by external sources of noise as the signal is closer to the noise floor.

There are many designs for photoacoustic cells. A selection of the cells are displayed in Figure 1.5; the Helmholtz resonator depicted in (b) is the most commonly used variety.

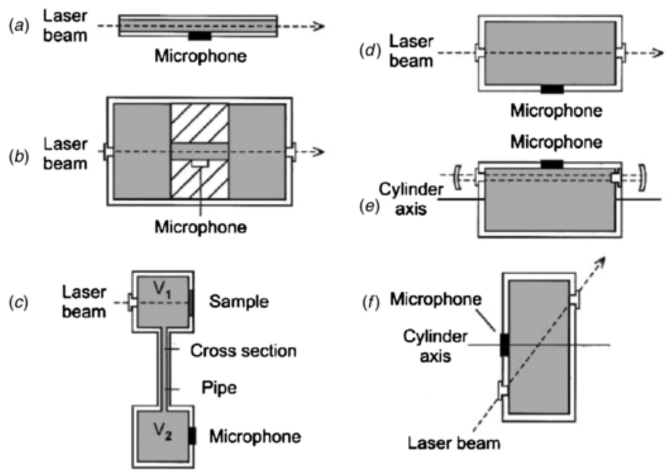

Figure 1.5: Common resonant photoacoustic cells (Miklós et al. 2001)

1.3 Literature Review

Photoacoustic spectroscopy (PAS) is a mature branch of metrology. The photoacoustic effect has been intensively researched for over 50 years, and the scientific community has been in general agreement on the theoretical underpinnings since Rosencwaig & Gersho (1976) published their seminal work 40 years ago. More recent developments in the field have concentrated mainly on methods of increasing the detection sensitivity; introducing quartz tuning forks (Kosterev, Tittel, Serebryakov, Malinovsky & Morozov 2005), interferometric displacement measurement (Koskinen et al. 2006), tuneable laser diodes (Besson et al. 2006), semiconductor quantum cascade lasers (Elia et al. 2009), and similar techniques.

The sensitivity of photoacoustic (PA) cells to ambient conditions is well understood (for example, (Kästle & Sigrist 1996, Miklós et al. 2001)). This occurs because the resonant frequency is dependent on the speed of sound inside the cell, and the speed of sound is directly affected by the temperature of the gas:

$$c = \sqrt{\frac{\gamma \cdot R \cdot T}{M}} \tag{1.1}$$

where

- c is the speed of sound in metres per second
- γ is the adiabatic index
- R is the molar gas constant
- T is the air temperature in Kelvin
- M is the molar mass

From Equation 1.1, given samples with identical constituent molecules, the speed of sound will vary as the square root of the absolute temperature; it changes by approximately $0.6\,\mathrm{m\,s^{-1}}$ for each $1\,^{\circ}\mathrm{C}$ change in temperature. Other physical artefacts that are noticeable in PA cells are the concentration of water vapour in the sample (positive correlation between the amount of water vapour and speed of sound), CO_2 concentration (negative correlation), and sound frequency (positive correlation). The gas composition also has an influence on the speed of sound; the adiabatic index in

Equation 1.1 is affected by the gas type, but has less effect on the speed of sound than does temperature.

With reference to PA cells, the usual solutions to altered sample conditions or compositions are to control the temperature of the sample and calibrate the PA cell at that temperature, or to build additional circuitry to track the resonant frequency and compensate accordingly (Angeli et al. 1991). Whilst these approaches are suitable for laboratory conditions, the additional cost, equipment size, and complexity demanded by these requirements are not feasible or economically viable for commercial use.

Later research began to focus more upon methods of using the characteristics of the PA cell and laser light source to locate the resonant frequency rather than external means of compensation. In 2001, Southwest Sciences Incorporated filed patents for phase locked and frequency locked PA spectrometers (Pilgrim, Bomse & Silver 2003*a*, Pilgrim, Bomse & Silver 2003*b*). In contrast to Angeli et al. (1991), their mechanism for frequency tracking did not require a separate acoustic source. Pilgrim's team modulated the frequency of the laser source to encompass the expected acoustic resonance of the cell, and then measured either the frequency of an odd harmonic (for frequency locking) or the phase angle of the sound relative to the modulation phase (for phase locking). The modulation frequency of the laser source would then be altered to match the detected resonant frequency. However, if the resonant frequency is initially undetermined, there is no signal to capture. Thus, a starting resonant frequency must be identified to a small margin of error by manual or automatic means. The technique is also limited by the laser technology being used; the span of modulation is not infinite. Advantages of Pilgrim's approach over previous methods include real-time resonance tracking and the ability to perform the monitoring and control in software.

Szakáll et al. (2009) took a similar approach with the introduction of the 'CHIRP' technique. Rather than sweeping around the modulation frequency, Szakáll's research group modulated the laser wavelength multiple times in a single excitation period. The Fourier transform of the resultant acoustic waveform was normalised against the Fourier transform of the applied laser modulation wavelengths, producing a clear representation of the resonant frequency. These three curves are shown in (b), (a), and (c) respectively in Figure 1.6.

The CHIRP technique produces excellent results under controlled conditions. The

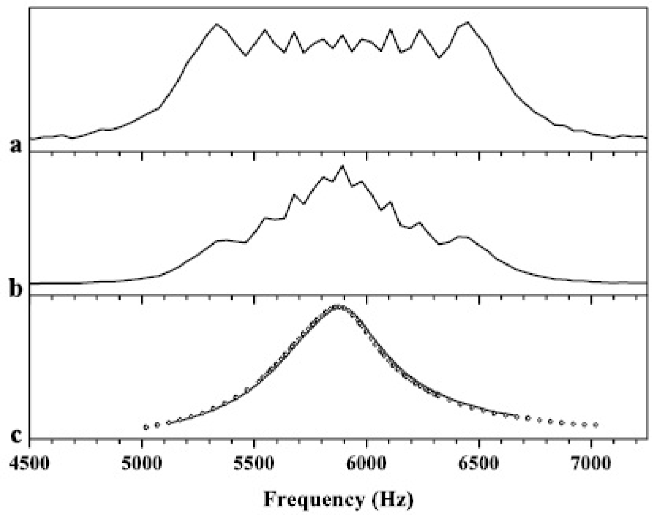

Figure 1.6: Modulated laser CHIRP, resultant acoustic waveform, and processed signal (Szakáll et al. 2009)

Fourier transforms required to be performed are not computationally expensive, and are easily realised in practice. The minimally-detectable concentration (MDC) of the sampled gas is reportedly unaffected by CHIRPing; this may be the case if a CHIRP falls on the resonant frequency, but may not be entirely correct if the resonant frequency is not stimulated. The linearity of the measurements, and consequently the absolute accuracy, may also be impacted if the laser is not modulated at the resonant frequency. Szakáll acknowledges that additional circuitry is required to drive the laser, and that the technique is only applicable to directly-modulated lasers, such as diode lasers. There may be additional issues if constituent gases have similar absorption frequencies, as the broad-spectrum CHIRP will be absorbed by all gases and may prevent the signal from the gases being differentiated.

Suchenek & Starecki (2011) continued in the same vein, using a square wave pulse rather than a continuously modulated laser signal. Although tests with samples were fairly successful, the technique is more applicable to characterisation of PA cells (determining the frequency response at all modulated frequencies) than in a practical installation. The duration of the applied square wave was critical to the resultant acoustic waveform; Figure 1.7 highlights signal abnormalities that are artefacts caused by differing pulse durations.

Suchenek makes no claims regarding the response of the cell to temperature variations. The process of determining the resonant frequency of a cell using the square wave pulse

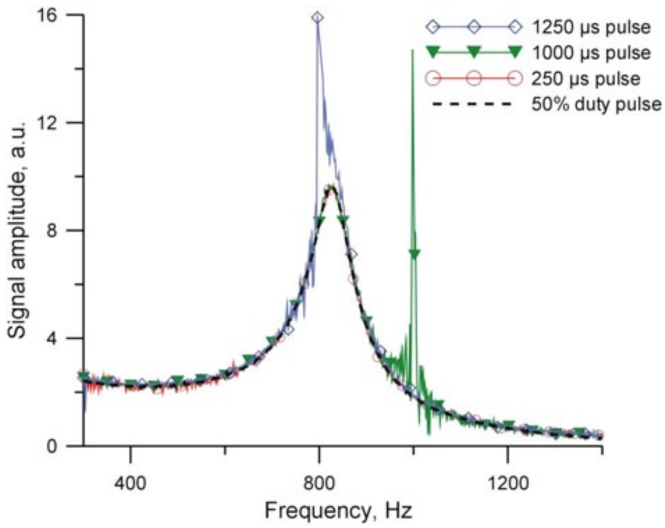

Figure 1.7: Corrected response of applied square wave (Suchenek & Starecki 2011)

is an improvement over point-by-point determination, and is simpler to implement than CHIRPing. However, the sensitivity to small changes in the applied signal duration is a serious drawback that cannot be overlooked.

Building on his previous work, Suchenek (2014) modified the square wave pulse to use superimposed sine waves as the source of the signal. In an example presented in the research paper, 376 measurements were made simultaneously to determine the resonant frequency between 500 Hz and 2 kHz with a 4 Hz resolution. This was accomplished by modulating the applied LED light source with 376 superimposed sine waves, each with an identical amplitude. The time- and frequency-domain plots of the applied signal are shown in Figure 1.8.

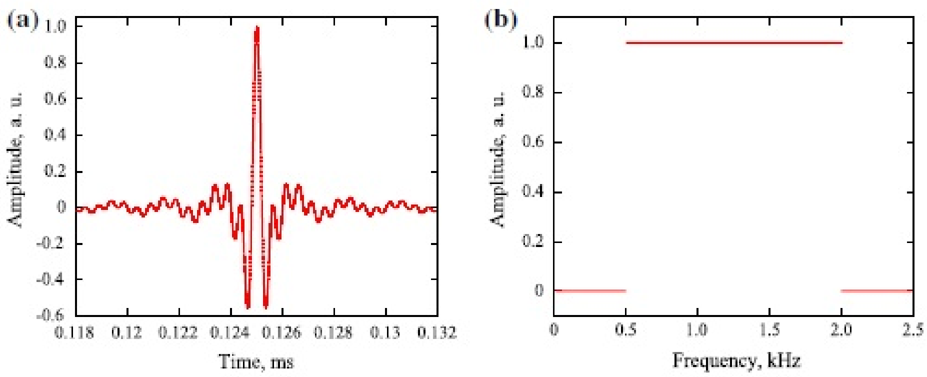

Figure 1.8: Time and frequency domain plots of superimposed sine waves (Suchenek 2014)

The use of superimposed sine waves improves on the square-wave technique as it removes the sensitivity to pulse length. Similarly to the previous research, this technique is currently aimed more at PA cell characterisation than designed for immediate implementation. The claimed measurement time for the 1.5 kHz bandwidth was 25 seconds, and the signal then had to be processed to identify the resonant frequency. Thus, the method of application for cell characterisation is not suited to a real-time sampling and analysis system. The response under varying temperatures was not investigated, nor was the response with multivariate sample gases.

1.4 Research Focus

The literature review has revealed some unique approaches to the determination of the resonant frequency of a photoacoustic cell. It has also revealed that there is currently very limited documented research available that ties together all the requirements for a robust, simple, real-time photoacoustic spectroscope.

Research will be focused on extending the existing research in the pursuit of a simple method of identifying the resonant frequency or frequencies of a photoacoustic cell in real time and under varying ambient conditions, most notably with variable temperature of the gas sample.

The result of the research is intended to be the detailed description of a technique that can be readily applied to a variety of light-source-agnostic PA cells, and an accessible algorithm for processing the acoustic signal. Other researchers should be able to implement and apply the results with a minimum of effort.

Chapter 2

Resonant Frequency Tracking Algorithm

The measured variable in a photoacoustic cell is the magnitude of the pressure change generated by the targeted sample fraction. The mechanism driving the creation of the pressure wave is detailed in section 1.2. When the modulation frequency is in the range audible to humans, a microphone can be used to detect the pressure change as an acoustic signal. The signal is detected in the time domain, and then converted to the frequency domain for inspection and analysis.

The acoustic signal, especially with low-Q photoacoustic cells, are very faint, and can be difficult to detect above the background noise level. To ensure that the signal is correctly identified, many repetitions of the waveform must be sampled and aggregated. As more repetitions are sampled, the accuracy of the result improves; the noise power averages to a low level across all sampled frequencies, and the power in the acoustic signal accumulates at the same frequency to give a strong signal proportional to the measured component.

There is a trade-off between measurement accuracy and speed of response – longer sampling periods positively correlate with improved accuracy. For very faint signals, thousands of cycles of the waveform may need to be sampled in order to definitively identify and ascertain the magnitude of the signal. If the frequency peak does not remain in the same position over the sampling period, the signals will be 'smeared' over a range of frequencies. In a real-time application, this is far from ideal. The sample temperature, pressure, and composition can all change rapidly, and under these circumstances, an extended sampling period will decrease the accuracy of the result.

The performance of the resonant peak tracking algorithm should not be impacted by any of these factors. Ideally, it will provide the correct frequency and magnitude of the target gas fractions under varying ambient conditions in real time. The design and testing of candidate algorithms is detailed in this section.

2.1 Effect of Temperature on Resonant Frequency

A simple acoustic resonator can be constructed from a straight, open pipe with length L and radius R, similar to the arrangement depicted in Figure 2.1. Kinsler, Frey, Coppens, & Sanders (2000, pp. 274) provide a proof that the first resonant frequency of this type of resonator is:

$$f_r = \frac{c}{2L_{eff}} \tag{2.1}$$

where c is the speed of sound and L_{eff} is the effective length of the resonator. The effective length accounts for the frequency distortion as the wavefront exits the pipe, and is defined as:

$$L_{eff} = L + \frac{8R}{3\pi} \tag{2.2}$$

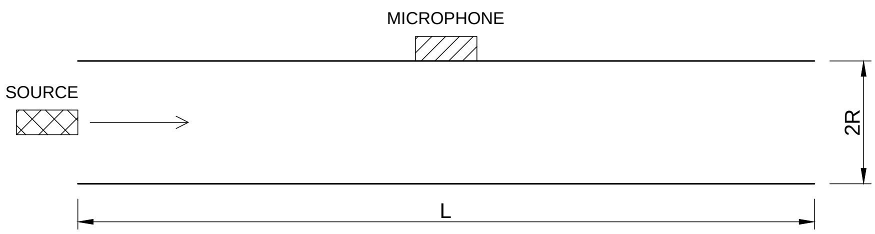

Figure 2.1: Simple acoustic resonator constructed from a straight length of pipe

Similarly, Starecki (2008) approximates the resonant frequency of a Helmholtz resonator as

$$f_r \approx \frac{cR}{2\pi}\sqrt{\frac{\pi}{L}\frac{V_1+V_2}{V_1V_2}} \tag{2.3}$$

where V_1 and V_2 are the volumes of the two cavities as shown in Figure 2.2.

By inspection of Equation 2.1 and Equation 2.3, the physical construction of the instrument is the major determinant of the resonant frequency of the cell. The speed

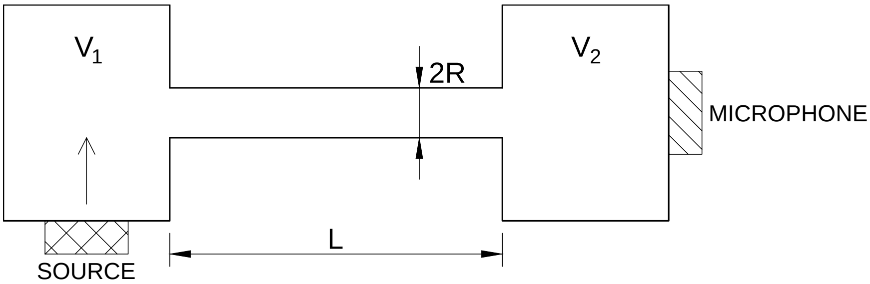

Figure 2.2: Simplified Helmholtz acoustic resonator arrangement

of sound, c, is the only parameter that is not dependent on cell design; the resonant frequency of the cell increases or decreases in direct proportion to the speed of sound.

The speed of sound is determined in accordance with Equation 2.4.

$$c = \sqrt{\frac{\gamma \cdot R \cdot T}{M}} \tag{2.4}$$

where

c = speed of sound, $\mathrm{m\,s^{-1}}$

γ = adiabatic index, ≈ 1.4 for diatomic gases and $= 1.\dot{6}$ for monatomic gases

R = molar gas constant, $8.3145\,\mathrm{J\,mol^{-1}\,K^{-1}}$

T = temperature, K

M = molar mass, $\mathrm{kg\,mol^{-1}}$

If we assume that the composition of the carrier gas is stable throughout the duration of the measurement, then the adiabatic index and molar mass will be constant. Relative stability of the carrier gas composition is not an unreasonable assumption. High-purity helium and nitrogen carrier gases are often used for laboratory experiments, and the addition or subtraction of a sample gas in the order of 100 ppm (0.01 %) will have a negligible impact on the molar mass or adiabatic constant. In the case of typical industrial process sampling, a large-scale change from diatomic to monatomic carrier gases is unlikely, and therefore the adiabatic index will remain relatively unchanged.

Displacement of atmospheric oxygen by another gas, such as carbon monoxide, carbon dioxide, or methane, will have an impact on the molecular weight of the gas passing through the cell. The speed of sound in dry air at 25 °C is $343.1\,\mathrm{m\,s^{-1}}$. Figure 2.3 illustrates the change in speed when oxygen in the carrier gas is displaced by 1000 ppm of a light gas, methane, or 1000 ppm of a heavy gas, carbon dioxide. These correspond with a change in the speed of sound to $344.1\,\mathrm{m\,s^{-1}}$ (0.28 %) and $342.4\,\mathrm{m\,s^{-1}}$ (−0.20 %) respectively.

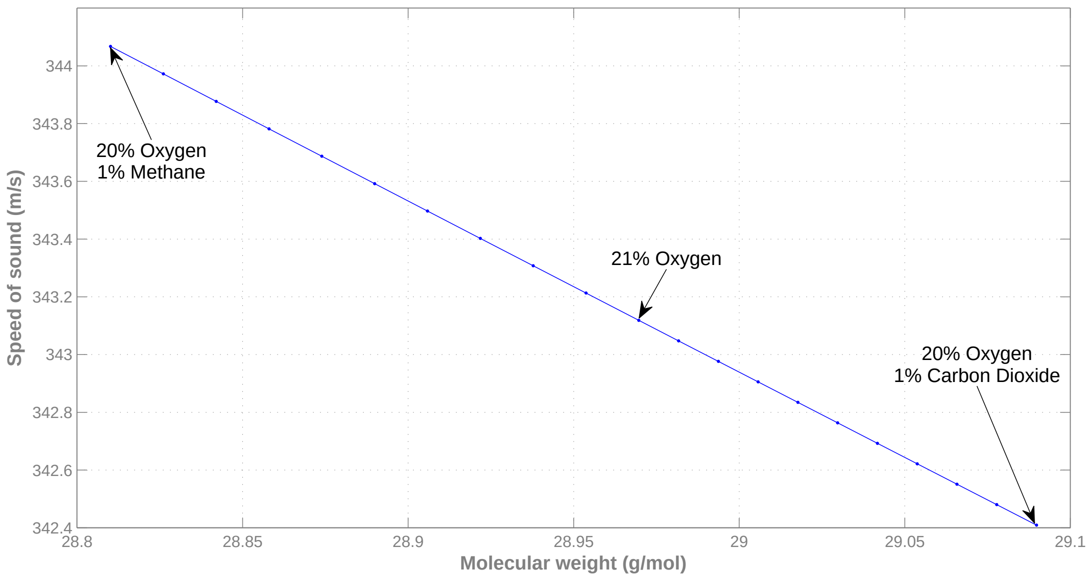

Figure 2.3: Change in speed of sound with varying molecular weight at 25 °C

The variation in the speed of sound due to the change of the composition of the carrier gas is, however, fairly insignificant when compared to that caused by heating and cooling of the sample, as illustrated by Figure 2.4. Applying Equation 2.4 with dry air as the carrier medium, the speed of sound increases from $331.2\,\mathrm{m\,s^{-1}}$ to $365.8\,\mathrm{m\,s^{-1}}$ over the range of 0 °C to 60 °C.

Consider this temperature variation applied to the open resonator of Figure 2.1 with a length L of 100 mm and radius R of 3 mm. Working through Equation 2.2 for the effective length,

$$\begin{aligned}
L_{eff} &= L + \frac{8R}{3\pi} \\
&= 100 \times 10^{-3} + \frac{8 \times 3 \times 10^{-3}}{3\pi} \\
L_{eff} &= 102.55\,\mathrm{mm}
\end{aligned}$$

and substituting this into Equation 2.1 which defines the relationship between frequency, cell length, and the speed of sound,

$$\begin{aligned}
f_{r(open)} &= \frac{c}{2 \cdot L_{eff}} \\
&= \frac{c}{2 \times 102.55 \times 10^{-3}} \\
f_{r(open)} &= 4.876c\,\mathrm{Hz}
\end{aligned}$$

Simlarly, for a Helmholtz resonator similar to that in Figure 2.2 with a length L of

25 mm, radius R of 6 mm, and volumes V_1 and V_2 of 12 270 mm^3:

$$\begin{aligned} L_{eff} &= L + \frac{8R}{3\pi} \\ &= 25 \times 10^{-3} + \frac{8 \times 6 \times 10^{-3}}{3\pi} \\ L_{eff} &= 30.09\,\mathrm{mm} \end{aligned}$$

$$\begin{aligned} f_{r(Helm)} &= \frac{cR}{2\pi}\sqrt{\frac{\pi}{L_{eff}}\frac{V_1 + V_2}{V_1 V_2}} \\ &= \frac{c \cdot 6 \times 10^{-3}}{2\pi}\sqrt{\frac{\pi}{30.09 \times 10^{-3}} \cdot \frac{2 \times 12\,270 \times 10^{-9}}{\left(12\,270 \times 10^{-9}\right)^2}} \\ f_{r(Helm)} &= 3.939c\,\mathrm{Hz} \end{aligned}$$

The frequency change in the open cell and Helmholtz resonator over the range of 0 °C to 60 °C are tabulated in Table 2.1.

Temperature (°C)	Speed of sound (m s^{-1})	Open cell f_r (Hz)	Helmholtz cell f_r (Hz)
0	331.2	1539.80	1304.56
5	334.2	1553.84	1316.46
10	337.2	1567.75	1328.24
15	340.2	1581.54	1339.92
20	343.1	1595.21	1351.51
25	346.0	1608.76	1362.99
30	348.9	1622.20	1374.38
35	351.8	1635.53	1385.67
40	354.6	1648.76	1396.87
45	357.5	1661.87	1407.98
50	360.3	1674.89	1419.01
55	363.0	1687.80	1429.95
60	365.8	1700.62	1440.81

Table 2.1: Photoacoustic cell resonant frequency sensitivity to temperature variations

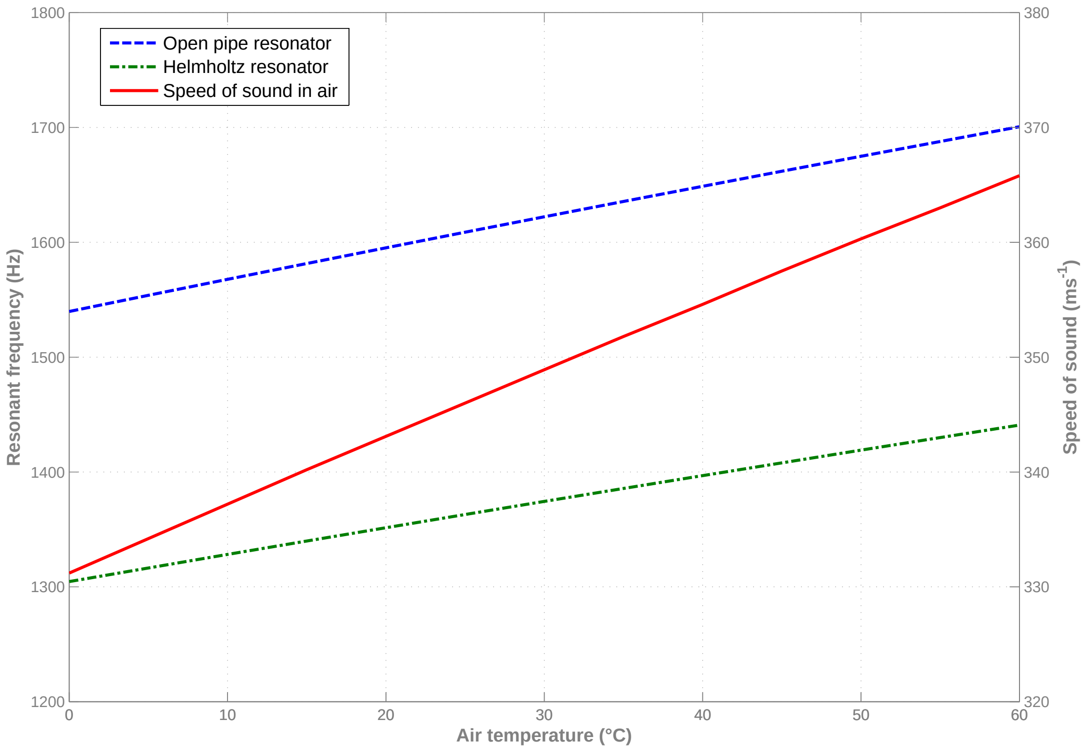

Figure 2.4: Change in speed of sound and resonant frequency shift with temperature change

2.2 Algorithm Development and Resonator Simulation

2.2.1 Model Constraints

Models of the physical characteristics and acoustic response of photoacoustic cells have been developed and proven by a succession of researchers – Bijnen, Reuss & Harren (1996) and Szakáll et al. (2009), for example. In contrast, the primary focus of this project is tracking a changing resonant frequency in a photoacoustic cell. Hence, defining a complete model of the cell and simulating the photoacoustic effect in detail is eschewed in favour of a model of the outputs of a theoretically perfect open-pipe cell. The simplified model assumes an equal gain across a broad range of frequencies, and ignores all perturbations of the system other than those attributable to frequency shift associated with changing temperature.

A variety of physical constraints shaped the development of the model. In order to verify the theoretically-determined performance of the algorithm, it had to be tested using a physical prototype. The prototype had to be able to be constructed in a domestic environment using basic hand tools and materials. The selection of equipment included hard-drawn copper tube and fittings, tube cutter, deburrer, brazing torch, silver solder, hacksaw, drill, and files. Although 6 mm copper tube would result in acoustic signal of greater amplitude than 12 mm tube, the difficulty of working with small-bore tube outside of a specialised workshop precluded use of this material.

The achievable temperature of the air entering the photoacoustic cell had to be limited to a range that could be safely created and controlled in a domestic environment. Lower and upper temperature limits of 0 °C and 60 °C respectively are easily achievable using ice and warm water baths, and abrogate the potential for personal injury from heat or cryogenic burns. Measurement repeatability is a key factor in validating the results; temperature control within the stated range can be achieved with the addition of ice or water, and can be accurately measured using an alcohol thermometer.

The mass-produced AM4010 microphones used for testing exhibit a flat frequency response over the range 200 Hz to 6000 Hz. Under 200 Hz, the gain varies from -50 dB to -60 dB; below this frequency, the amplitude of the measured signal is a function of both the frequency and the power of the incident wave. Operation in this non-linear region would complicate analysis of the signal, and is avoided by moving the frequency to well within the area of flat response. With reference to Table 2.1, the 'centre frequency' corresponding to room temperature for the open cell is approximately 1600 Hz, with a window that extends about 100 Hz in either direction for the upper and lower temperature limits. Consequently, the acoustic signal of the open cell resonator is expected to fall within the linear gain region of the microphone throughout the nominated temperature range.

The rate of change of temperature, from ambient to the high or low temperature limits, is dependent on many factors; heat transfer coefficient from water to air through copper, the wall thickness of the copper tube, length of piping, pipe diameter, ambient temperature, velocity of gas in the pipe, roughness of the pipe walls, and so on. Modelling the rate of change of temperature is complicated, and cannot be accurately measured to reflect all possible circumstances. Temperature equilibrium between the water bath and the sample gas occurred in the order of tens of seconds in preliminary experiments; allowing for a rate of change of temperature of 5 °C per second could reasonably be expected to cover the most radical excursions.

MATLAB was chosen as the platform for signal capture and analysis. The software package is widely used in industry and academia, ensuring that algorithms developed could be checked, verified, and reused with a minimal degree of effort. The MATLAB toolboxes expose a simple method of implementing some advanced and niche functions which are useful in digital signal processing. There is also an active MATLAB user community, providing a platform to raise questions regarding software functionality and discuss any problems encountered. Finally, MATLAB can be used to complete all functions required for this project; audio capture, audio playback, signal processing, file access, and data presentation.

The literature review identified that there was uncertainty in the scientific community as to the relative merits of the Least Mean Squares (LMS) and Fast Fourier Transform (FFT) algorithms for signal analysis. The most definitive answer was provided by Starecki & Owczarek (2007), who reported that the signal to noise ratio and error rates were the same when either FFT or LMS were used for amplitude calculations. They suggest that LMS should be used preferentially as it is more computationally efficient than FFT. However, utilising MATLAB's inbuilt FFT function would remove one potential source of error, and the performance of the FFT in the simulation environment was not sufficiently poor that seeking an alternative was deemed necessary.

A single computer was employed for model development, simulation, data collection, and signal processing. The functions were generally performed sequentially rather than concurrently, limiting cross-function performance impact and resource contention. Using additional computer hardware would have increased the project complexity without a concomitant increase in speed or accuracy of the results. Key specifications of the computer include:

- Asus P8P67 mainboard
- Intel Core i7-2600K processor
- Realtek HD Audio, max. 16 bit, 192 kHz for recording and 24 bit, 192 kHz for playback
- 16 GiB RAM
- Windows 7 Ultimate, 64 bit
- MATLAB Student Edition R2010a, v7.10.0.499

As the target resonant frequency range is approximately 1500 Hz to 1700 Hz, a sample rate of 192 kHz can justifiably characterised as excessive. The minimum recording sample rate of the hardware and software is CD quality – 16 bit at 44 100 Hz. This will sample the audio signal at least 25 times per cycle, and strikes a balance between the signal resolution achieved and the size of the audio files to be processed. Array sizes were a very real and ever-present consideration during development of the model and algorithms. MATLAB Student Edition is 32-bit only, limiting the amount of computer memory that MATLAB will utilise. The maximum array sizes is determined using the command `memory` in the MATLAB development environment. On the development computer, this command returned:

```
EDU>> memory
Maximum possible array:               2046 MB (2.146e+009 bytes) *
Memory available for all arrays:      3470 MB (3.638e+009 bytes) **
Memory used by MATLAB:                 305 MB (3.199e+008 bytes)
Physical Memory (RAM):               16364 MB (1.716e+010 bytes)
```

The default `double` (double precision floating point) data type in MATLAB uses 8 bytes of memory, limiting the largest array to a maximum of around 275 million elements. In practice, the total memory available to MATLAB is a more restrictive limiting factor in determining maximum array sizes; multiple temporary arrays are created as the audio is captured and processed, and each array depletes the total memory pool available. 'Out of memory' errors were constantly encountered during the development phase, necessitating the implementation of short-duration audio files and FFT buffering, and limiting the overlap when windowing frames. Commercial versions of MATLAB would, in all likelihood, avoid these issues through the ability to address a larger memory space.

The model, algorithms, and simulations were developed with consideration of the above constraints, leading to the following key resonator model and simulation parameters being selected:

- 1600 Hz centre frequency
- 200 Hz frequency range
- 15 Hz per second frequency change ($\approx 5\,°\mathrm{C}$ per second)
- 44.1 kHz audio sampling rate

2.2.2 Base Frequency FFT

To ensure that MATLAB's FFT was being applied and interpreted correctly, the output of several simulations with a known outcome were examined.

The first simulation was of a noiseless 1600 Hz sine wave with an amplitude of 1 unit, sampled at 44.1 kHz over a period of 1.6 seconds. The expected output was an FFT with a single discrete peak at 1600 Hz. The first three cycles of the sine wave are shown in Figure 2.5, and the corresponding FFT is shown in Figure 2.6. The amplitude of the FFT is 1, as expected, as there are no other frequencies present in the sine wave.

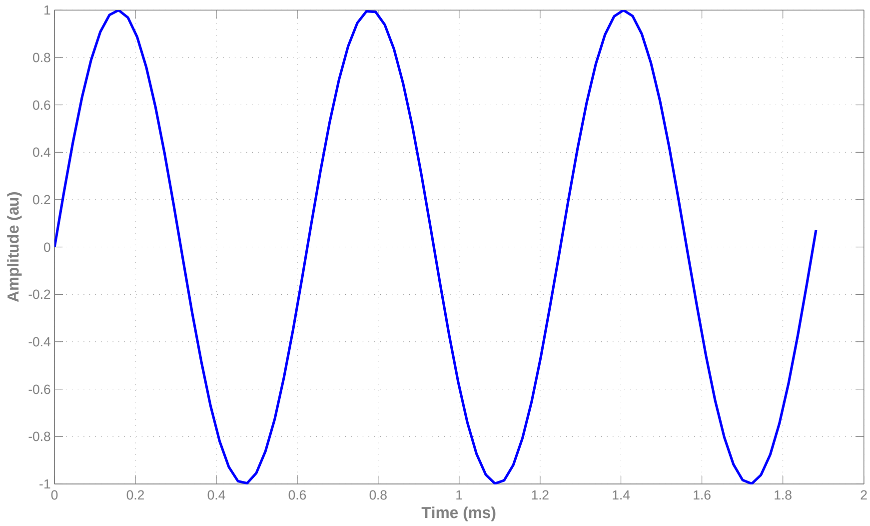

Figure 2.5: Simulated pure 1600 Hz sine wave sampled at 44.1 kHz

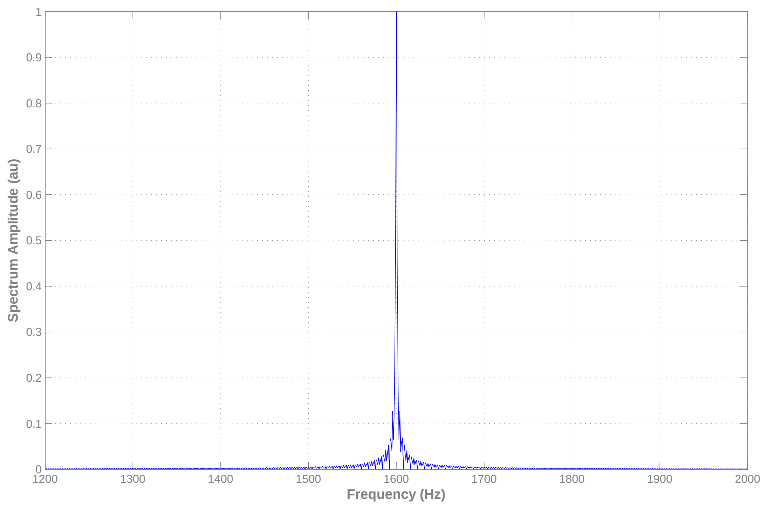

Figure 2.6: FFT of pure 1600 Hz sine wave sampled at 44.1 kHz

The second simulation used the same 1600 Hz sine wave with the addition of white noise. The period and sample rate were maintained at 1.6 s and 44.1 kHz respectively. As only one sinusoid was present in the waveform, the FFT was again expected to have a single peak at 1600 Hz, together with random noise spread evenly across all other frequencies. This expectation was borne out by the results shown in Figure 2.7 and Figure 2.8. The signal to noise ratio of the waveform in these plots was −20 dB; the signal in Figure 2.7 is indicated by the dashed line, with the solid line representing the signal with added noise.

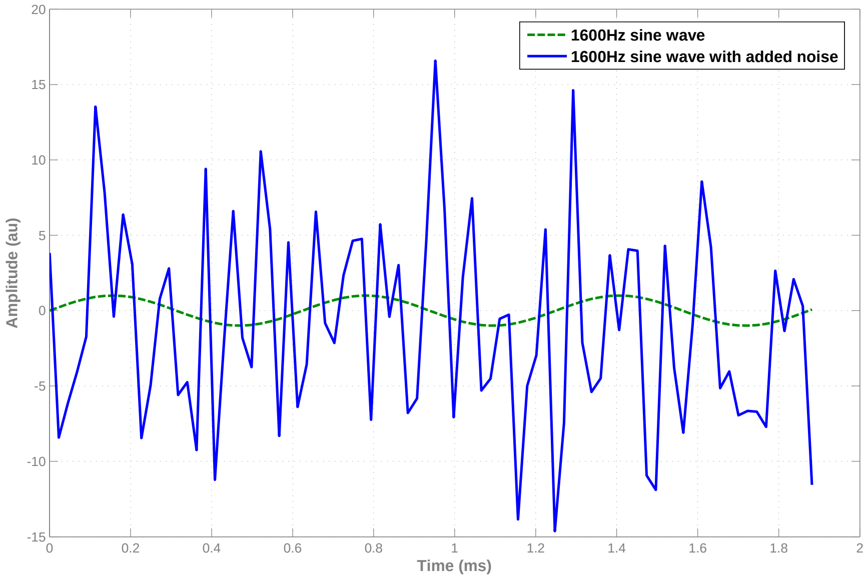

Figure 2.7: Simulated 1600 Hz sine wave with noise sampled at 44.1 kHz

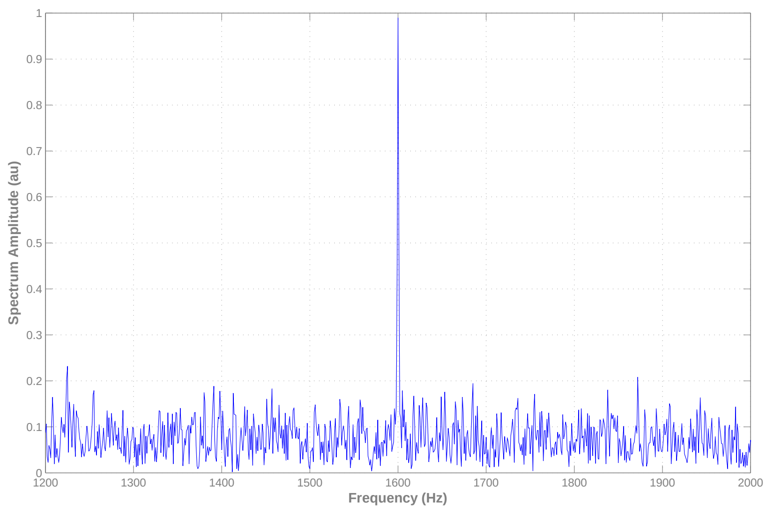

Figure 2.8: FFT of 1600 Hz sine wave with noise sampled at 44.1 kHz

These two test cases were sufficient to prove the operation of the logic with a sine wave at a fixed frequency.

2.2.3 Variable Frequency FFT

The next step in the development of the frequency tracking algorithm involved applying an FFT to a sine wave with a changing frequency. This is known as a 'chirp' signal, referring to the sound of a bird's chirp. A chirp signal with a length of two seconds was created, with a starting frequency of 1600 Hz and a rate of increase of 15 Hz per second, corresponding with the design parameters previously discussed.

The result of applying an FFT to the chirp signal is shown in Figure 2.9; it exhibits large peaks near the initial and terminal frequencies, with lower-amplitude ripples joining the two peaks.

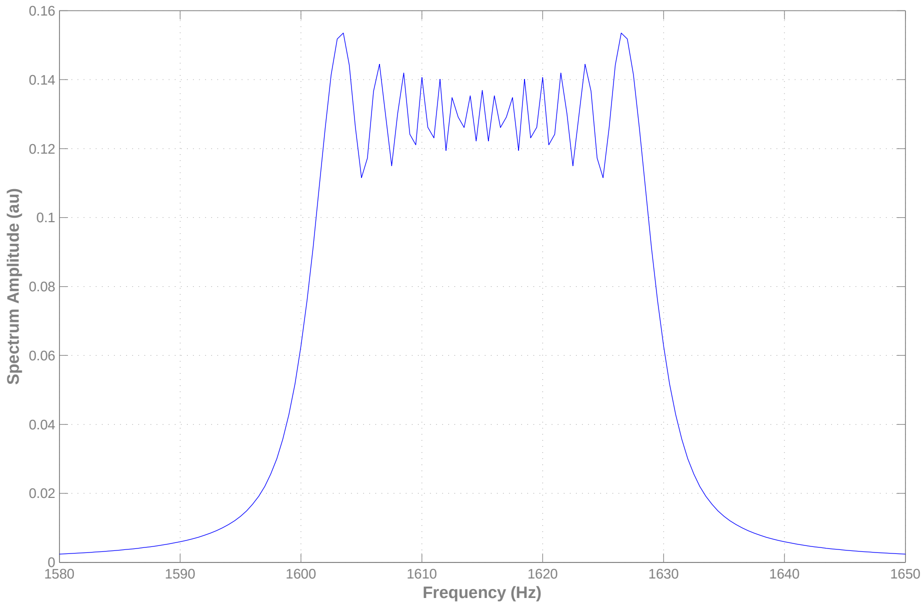

Figure 2.9: FFT of 1600 Hz to 1630 Hz chirp signal

The FFT of the two second chirp signal, processed as a single vector, has components smeared across the frequency spectrum. In Figure 2.9, the peak amplitude of 0.1535 occurs twice, at 1603.5 Hz and 1626.5 Hz; the average of the amplitudes of the elevated frequencies is 1615 Hz. Neither the peak values nor the average value conveys any information about the change in the frequency over time, instead summarising the chirp frequency spectrum into concise values lacking meaning and context.

A spectrogram function was applied to analyse the chirp signal. The output of the spectrogram is a plot displaying the peak frequency and amplitude of a signal over time. However, the result did not have sufficient resolution to discern the frequency with any degree of accuracy, and therefore, another method of determining the time vs. frequency relationship was required.

Rather than importing the signal and processing it in a single FFT operation, the signal vector can be windowed into frames, and an FFT applied to each frame. The process of applying a window with a 50% overlap to a waveform is graphically depicted in Figure 2.10.

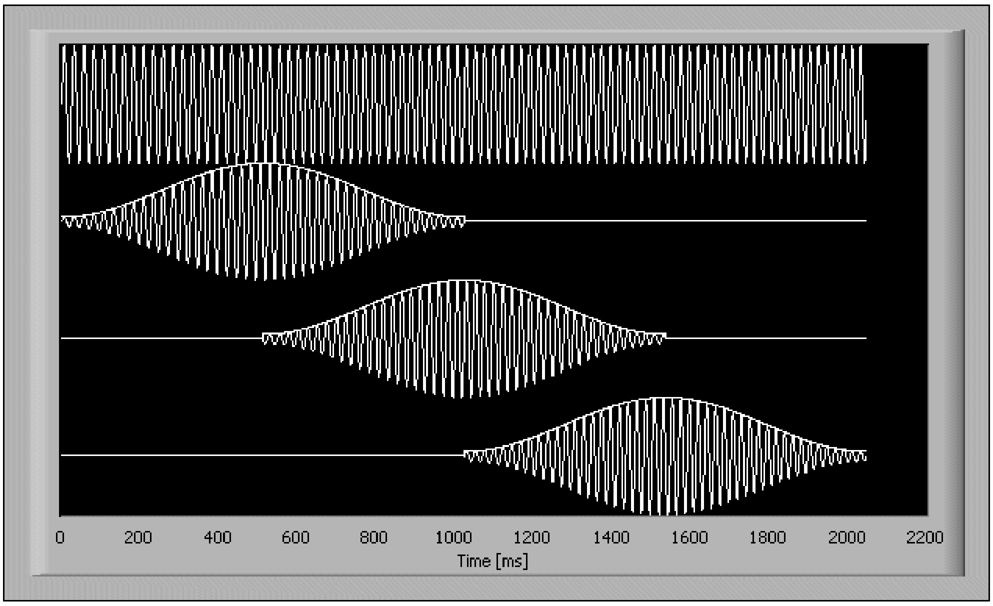

Figure 2.10: Example of FFT window application (National Instruments 2009)

By picking the maximum value from each FFT window, and determining the size and overlap of each window, a chart of the change in frequency over time can be developed. This is illustrated in Figure 2.11; a Hamming window of 4410 samples and an overlap of 10% (441 samples) is applied to a chirp signal that increases in frequency from 1600 Hz to 1615 Hz over a period of one second. The time-frequency chart has 10 values with 10 ms between samples.

The discontinuities in the frequency tracking are readily distinguishable. These are due to the amplitude distortion caused by the application of the window; the amplitude of the values at the edges of the window are attenuated more than those in the centre, thereby weighting the signal toward the frequency at the centre of the window. This can be partially remedied by decreasing the window size (see Figure 2.12a, where the window size was reduced to 2205 samples), or by increasing the window overlap (as shown in Figure 2.12b, where the 4410 samples were overlapped by 25%). Increasing the overlap has a better result in terms of the smoothness of the tracking chart, and

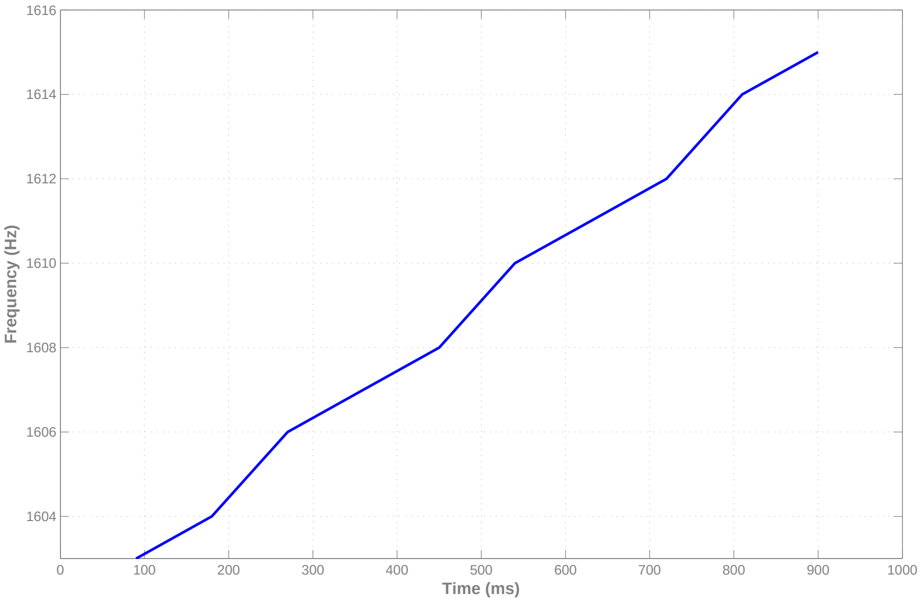

Figure 2.11: Frequency tracking chart using a Hamming window of 4410 samples and 10% window overlap

is less computationally expensive than decreasing the window size by a large amount. In the examples in Figure 2.12a and Figure 2.12b, increasing the overlap requires 12 FFTs to be processed, whereas the smaller window is achieved using 21 FFTs.

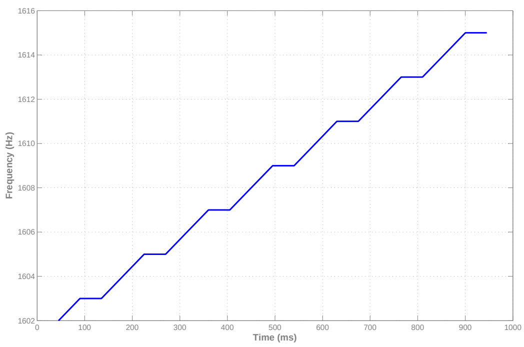

(a) 2205 samples, 10% window overlap

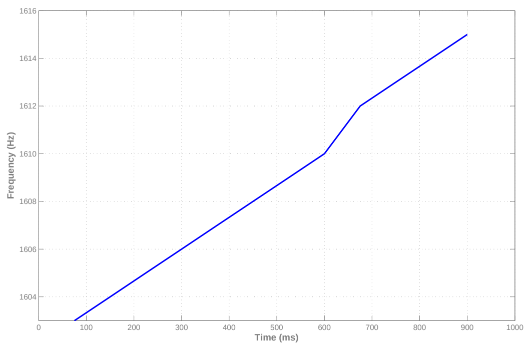

(b) 4410 samples, 25% window overlap

Figure 2.12: Frequency tracking with different size Hamming windows

When the chirp frequency is increasing or decreasing smoothly, the signal discontinuities in the time vs. frequency chart are minimal. However, if the signal frequency stops changing, or alternates between increasing and decreasing frequency, there can be large instantaneous peaks and troughs in the maximum frequency. This is caused by phase change in the signal at the points where the overlaps occur, resulting in cancellation or reinforcement of the stitched edges of the signal window. The discontinuities are visible in Figure 2.13a; the frequency is increased from 1600 Hz to 1615 Hz over a period of one second, held at 1615 Hz for one second, and finally decreased back to 1600 Hz over one second. The Hamming window used for Figure 2.13a was 4410 samples in length, and had an overlap of 441 samples.

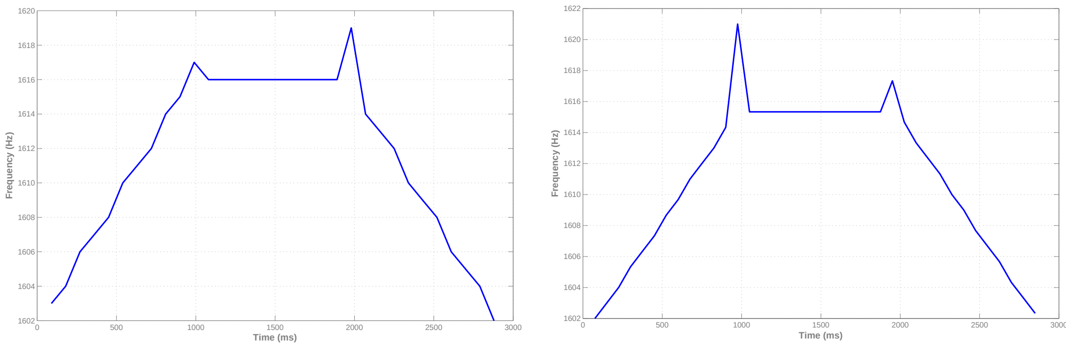

(a) 4410 samples, 10% window overlap

(b) 4410 samples, 25% window overlap

Figure 2.13: Three-segment frequency tracking charts with Hamming windows

In this case, increasing the overlap from 10 % to 25 % does not alleviate the problem, as can be seen in the time vs. frequency chart in Figure 2.13b. In this instance, increasing the overlap has exacerbated the problem, and the amplitude of the frequency spike at the points where the frequency changes has increased rather than smoothed out.

As the frequency changes are minimal, and the wave amplitudes are the same across all frequencies, the peaks can be minimised by using a rectangular window. This is the equivalent of buffering the data into windows, and not attenuating the amplitude of the samples inside the window. By making the window size large enough to contain roughly four complete cycles of the 1600 Hz waveform, there are sufficient samples to create a representative FFT whilst simultaneously preventing the discontinuities caused by reinforcement and cancellation of overlapped waveforms. The resultant time vs. frequency waveform using a rectangular window with no overlap is shown in Figure 2.14, exhibiting a smooth, even change in frequency between each 143 ms time point.

In summary, the best simulation algorithm to allow for tracking the frequency change over time was splitting the waveform into chunks containing approximately four complete cycles of the target frequency using a rectangular window, and processing each chunk with an FFT. This gave a good representation of the dominant frequency in each chunk, and prevented discontinuities at the points where the frequency stopped changing, or where it reversed direction between an increasing and decreasing frequency.

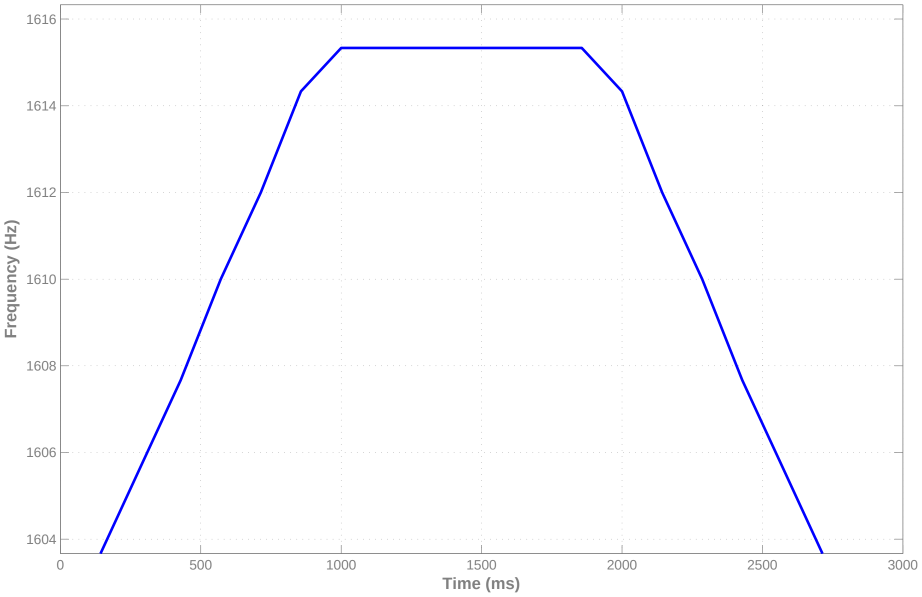

Figure 2.14: Three-segment frequency tracking chart using a rectangular window of 6300 samples and no overlap

Chapter 3

Resonator Prototype

Development of the algorithm provided a theoretical framework for the frequency tracking in a photoacoustic resonator. Theories, however, are not necessarily borne out when applied in practice. The performance of the algorithm, and any required refinements, can only be categorically determined through testing with a physical model.

The fundamental focus of the research was not in the creation of the acoustic pressure wave, but rather in the measurement of the changing acoustic signal. To this end, instead of creating the acoustic signal with a laser, a speaker was used to introduce the sound wave from the position where the laser would normally be located, as depicted in Figure 3.1.

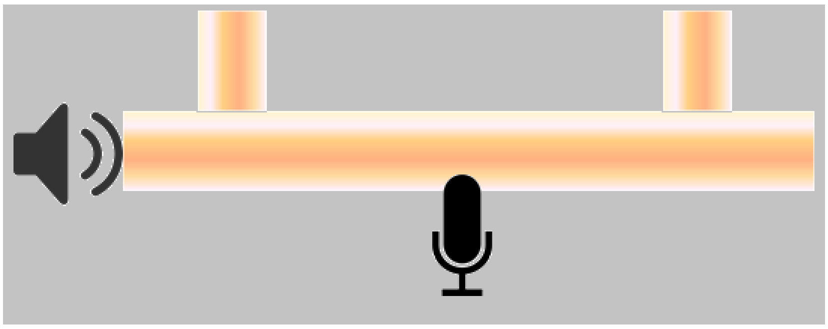

Figure 3.1: Replacing laser with speaker in resonator assembly

This arrangement is not ideal; it does not unambiguously replicate the signal that would be originate from a laser, especially with respect to the amplitude and phase of the acoustic wave and the precise response to the constituent gases. Conversely, the main advantage of using a speaker is that uncertainties created by the introduction of a laser can be avoided; there are no issues with calibration of the wavelength, power output, pulse width modulation, temperature stability of the laser circuitry, and so on.

Use of the speaker reduces the experimental variability to a minimum - a known frequency is directly produced to be detected by the microphone. This approach removes most of the uncertainty from the testing process, allowing the focus to remain on verifying the applicability and performance of the algorithm.

3.1 Materials and Construction

As discussed in section 2.2.1, the resonator simulacrum had to be constructed in a small, rudimentary home workshop where a minimal amount of tooling was available. This provided significant constraint on the materials of construction and the methods for handling them.

For example, a stainless steel tube with a 3 mm or 6 mm bore would have been ideal to use as the resonator tube, but the difficulty in drilling and deburring holes for gas entry and exit and polishing the internal surface of the tube rendered this option impracticable.

A similar problem was encountered with the electronic components. The smallest off-the-shelf speaker exhibiting a reasonable frequency range had a diameter of 25 mm, and miniature microphones were available with a 6 mm diameter as a minimum. Ideally, these components would have only been half this size to better fit the mechanical components and reduce protrusion distances.

The design of the prototype was, therefore, a compromise between the desired performance, material availability, and manufacturing constraints. A dimensional drawing of the resonator design is shown in Figure 3.2. The PVC tubing and electronic components have been omitted for clarity.

The resonator body was constructed of 12 mm hard-drawn copper tube. The speaker was attached using a 12 mm to 25 mm reducer, silver soldered to the resonator body. The gas take-off points were 12 mm tees, cut in half and attached to the resonator body with silicone adhesive. The tees are designed to be soldered to the ends of a pipe, but

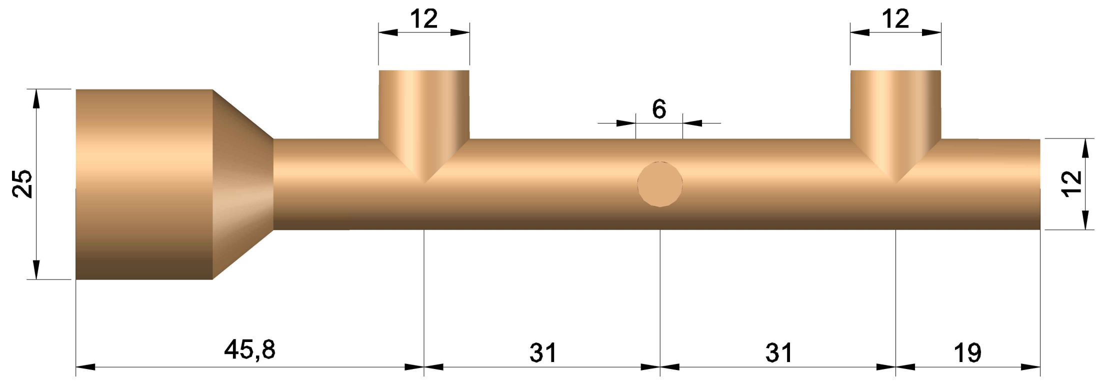

Figure 3.2: Dimensional drawing of resonator prototype (all dimensions in millimetres)

cutting the resonator body into sections would have created internal pipe obstructions which would disturb the acoustic signal. All holes were cleaned and deburred both internally and externally, and the inside of the copper pipe was polished using glass paper.

The microphone was press-fitted into a 6 mm hole drilled 50 mm from the open end of the resonator tube, and the speaker was mounted on the 25 mm socket. Both the microphone and speaker were soldered to 3.5 mm mono audio connectors using low-loss cable.

Flexible PVC tubing was fitted to the gas entry and exit tees. The gas entry tube was spliced to a section of 12 mm copper tube approximately 500 mm from the tee to assist with heat transfer from the water bath to the sample gas.

The whole assembly was placed in a box which was covered internally with sound dampening foam. The acoustic tiles were intended to limit sound transfer from external sources to the microphone mounted in the resonator.

A photograph of the completed prototype is shown in Figure 3.3. The speaker is on the left of the photograph, and the microphone is toward the centre. The clear PVC pipes transporting the sample gas to and from the the resonator are located in the tees at the top of the photograph. The wooden jig keeps the assembly in a fixed position, and ensures that the distance between the speaker and the resonator tube is maintained.

Prior to commencing the construction process, a Job Safety Analysis (JSA) was undertaken. The completed JSAs for the mechanical and electrical construction tasks are contained in Appendix B. The JSA details the hazards associated with the resonator

Figure 3.3: Fully assembled prototype resonator used for testing)

manufacture, defines controls implemented to reduce the severity or remove the identified hazards, and assigns a residual risk score which indicates whether further controls are required, or if the controls applied are sufficient to allow the job to proceed.

3.2 Frequency Response Curve

Prior to using the speaker and microphone in the resonator, the combined frequency response curve had to be determined. If the frequency response was not substantially flat across the measurement range, the validity of the results would be questionable.

The speaker was a Jaycar Electronics part number AS3030. The manufacturer data sheet for this component shows that the speaker output is approximately 80 dB across the frequency range 300 Hz to 10 000 Hz. The frequency response curve from the data sheet for the microphone, a Jaycar Electronics part number AM4008, was illegible. A slightly higher quality data sheet sourced from the Australian distributor suggests a flat response from 100 Hz to 900 Hz, followed by a steep drop in sensitivity of around

10 dB from 900 Hz to 1100 Hz, and then a flat response again from 1100 Hz to 5000 Hz. The manufacturer data sheets are included in Appendix D.

The microphone and speaker were placed in the acoustically-isolated box 80 mm apart, matching the separation distance in the resonator. The two components were oriented to face each other such that the sound wave from the speaker was perpendicular to the microphone face. The speaker played a chirp, ascending from 500 Hz to 2500 Hz over a period of 20 seconds, whilst simultaneously being recorded by the microphone. The 500 Hz to 2500 Hz bandpass filter displayed in Figure 3.4 was applied to the audio signal to attenuate spurious signals from outside this range.

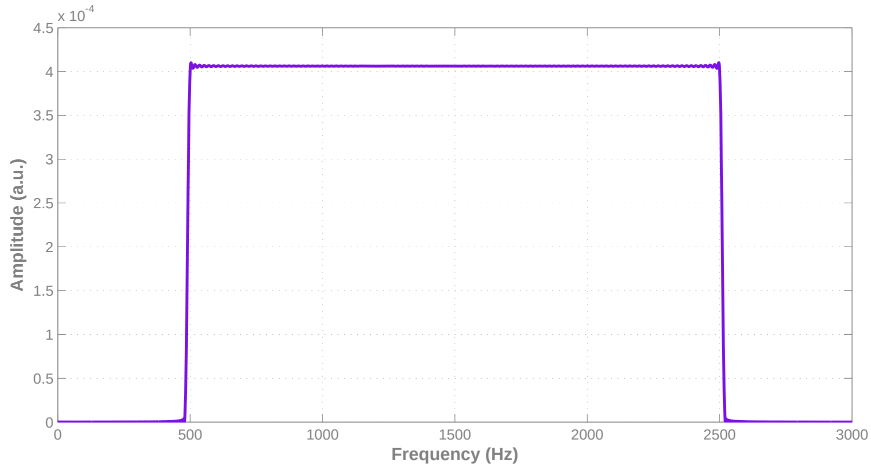

Figure 3.4: 500 Hz to 2500 Hz bandpass filter used for initial testing

An FFT of the resultant waveform was created to determine the relative amplitude in the frequency domain. The measurement process was repeated five times to reduce the impact of one-off disturbances in the captured audio. The five FFTs were averaged and plotted, and it was immediately apparent from the result shown in Figure 3.5 that there was an issue with the experimental setup.

Although the signal was not expected to be completely flat, the extent of the variability across the measured range was extreme. In some cases, the amplitude of consecutive samples in the FFT varied by an order of magnitude. A 10 Hz running average signal is displayed as the red line superimposed on Figure 3.5, and the samples in the FFT would be expected to be clustered more closely around this point.

After some investigation and repeated trials, several adjustments were made that resolved the problems previously noted:

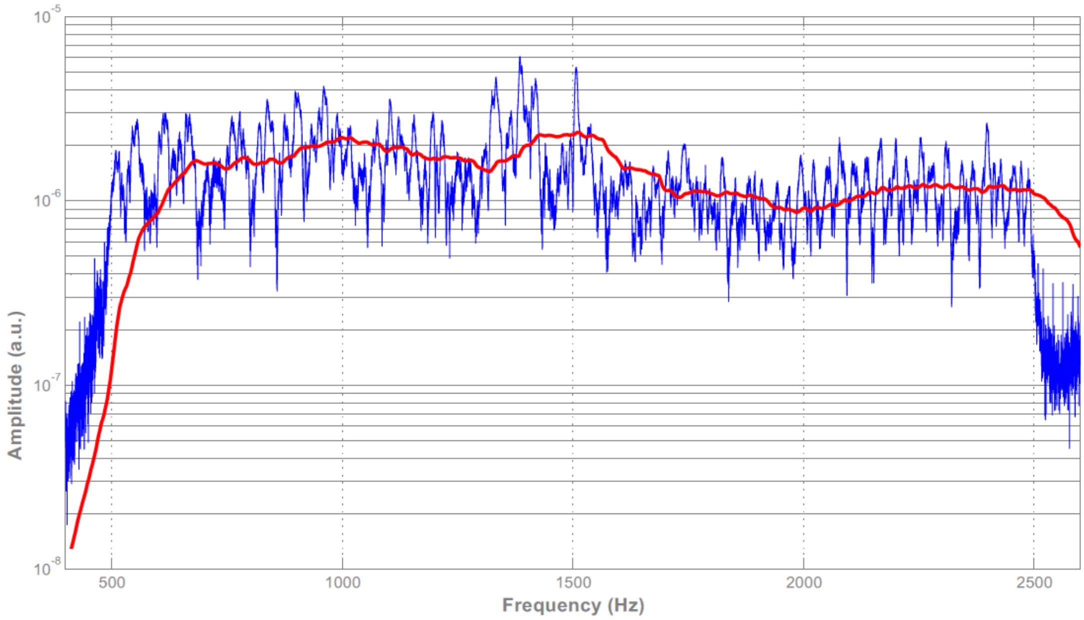

Figure 3.5: Initial microphone and speaker frequency response curve without resonator

1. The speaker was moved slightly clear of the socket rather than being pressed hard up against it, as the movement of the speaker cone was being retarded by the socket and consequently damping the audio signal.

2. The virus scanner on the computer was modified to exclude the MATLAB executable from being scanned in real time, which had impacted the data collection process.

3. The recording configuration on the computer (Figure 3.6) was changed to deactivate both noise suppression and acoustic echo cancellation in the audio manager.

Of the three changes listed above, the last had the most impact on the signal. During iterative testing to diagnose the problem, a static 1600 Hz sine wave was used to check the response after each change was made. The first one or two cycles of the waveform were always present in the recorded signal, but the remainder of the 1600 Hz signal was completely suppressed by the noise cancelling circuitry on the sound card, and was indistinguishable from the noise floor. The chirp signal was suffering the same problem due to the slow rate of change of the chirp, with roughly 1 in 20 cycles of the chirp waveform present in the recorded audio stream before being removed by the noise cancelling hardware. Once this option was deselected, the signal was clearly present for the entire length of the recording.

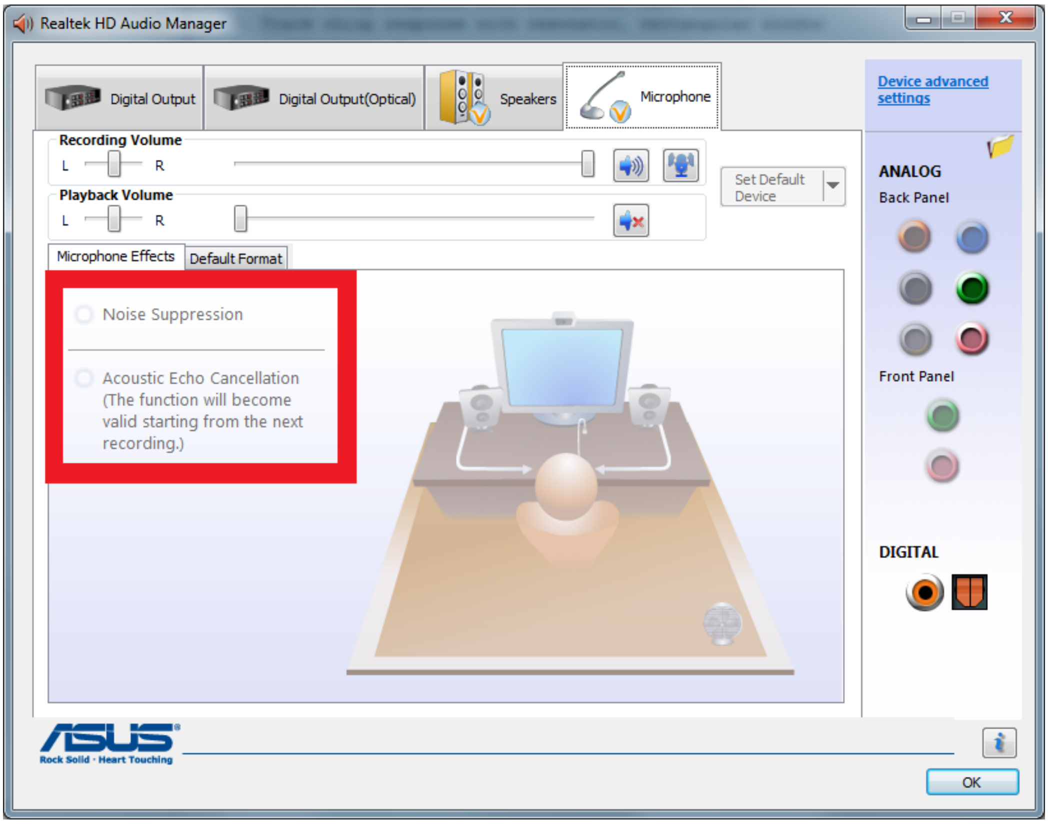

Figure 3.6: Computer audio manager application - noise suppression and echo cancelling on microphone

Following the implementation of the above changes, the process of establishing the combined speaker and microphone frequency response curve was restarted from the beginning. The same 20 second duration chirp increasing from 500 Hz to 2500 Hz was again recorded and filtered five times consecutively. The FFTs were averaged and plotted, resulting in the frequency domain graph shown in Figure 3.7.

The amplitude is effectively flat across the 500 Hz to 2500 Hz frequency range, with no major excursions or deviations immediately apparent in the signal. The higher density of points in the FFT of Figure 3.7 compared with that of Figure 3.5 is indicative of the effectiveness of the hardware noise cancelling which had suppressed the signal in the initial round of testing. The frequency response of Figure 3.7 was sufficiently narrow that results of further tests could be ascribed to physical phenomena rather than equipment artefacts.

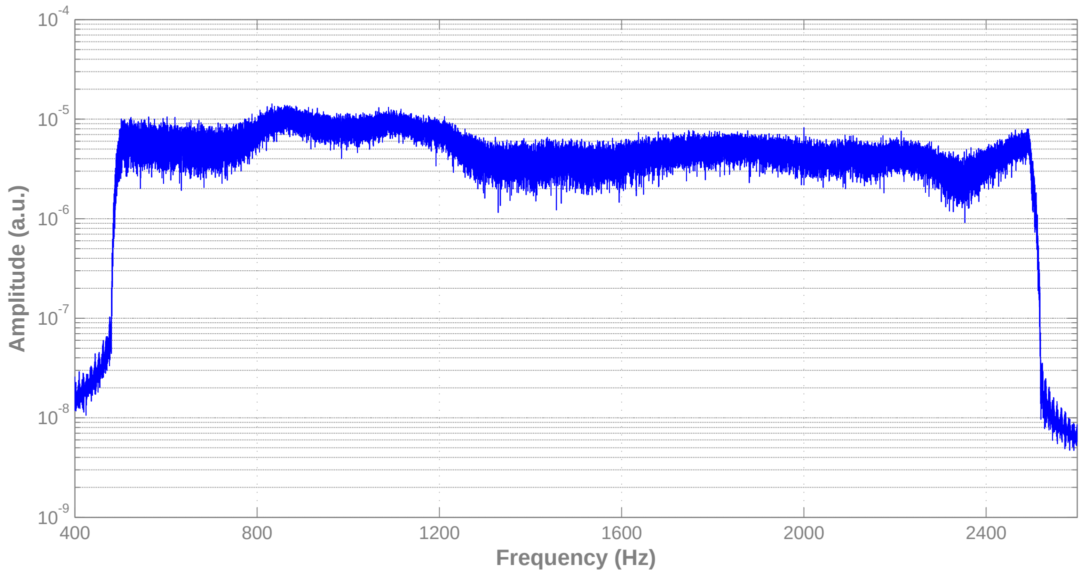

Figure 3.7: Combined microphone and speaker frequency response curve without resonator

3.3 Fixed Sine Wave Response with Resonator

The next stage in the testing process involved installing the microphone into the resonator, and determining the response at a fixed frequency.

Assembly of the prototype was completed with the microphone being pressed into place in the resonator. A fixed 1600 Hz sine wave was played through the speaker, and the recording from the microphone was analysed with an FFT prior to the application of a filter. As with the initial testing, this process was repeated several times to test the repeatability of the results.

The frequency domain plots revealed substantial variability in the audio signal. Significant signal power was present at the second and third harmonics (3200 Hz and 4800 Hz respectively). The speaker volume was reduced from 90% to 80%, and the FFT of another 1600 Hz sine wave was examined with positive results. The second harmonic had disappeared when the FFT was viewed on a linear scale, and the third harmonic had been drastically attenuated. The audio volume was further reduced to 60%, with the end result that only the fundamental frequency was visible on an FFT with a linear scale.

As shown in Figure 3.8, frequencies of 3200 Hz and 4800 Hz are discernible when the values are plotted on a logarithmic scale, but they are three orders of magnitude lower

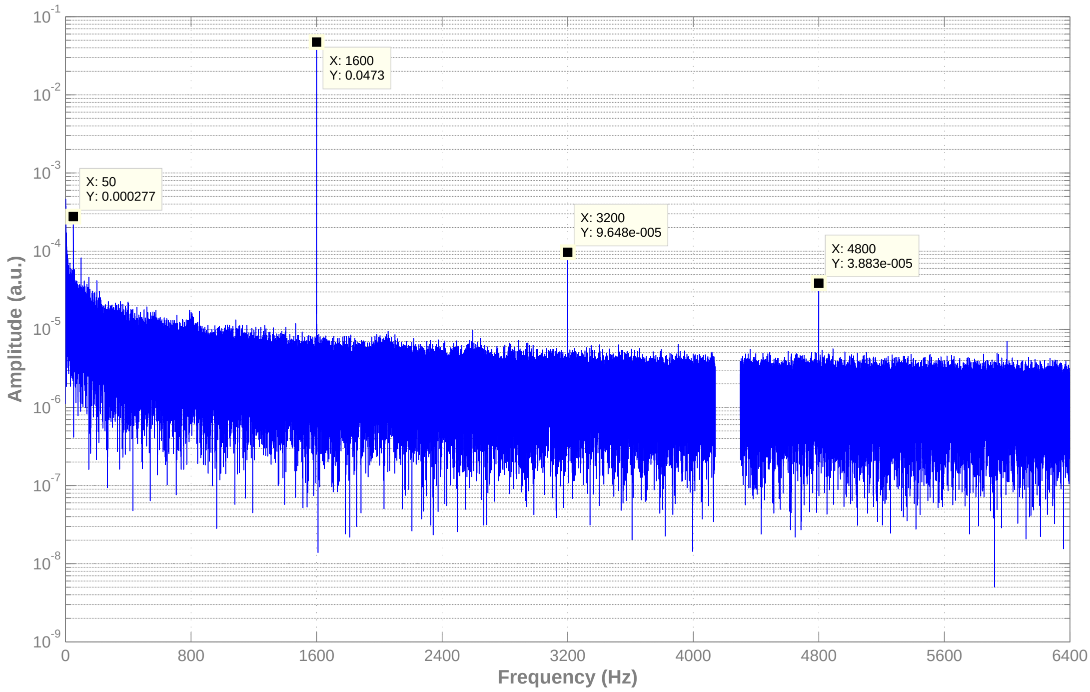

Figure 3.8: FFT of 1600 Hz audio wave from resonator

than the 1600 Hz signal. Additionally, the powerline frequency of 50 Hz has an elevated amplitude in the FFT, probably introduced into the measured signal courtesy of insufficient shielding on the microphone cable.

The magnified section of the FFT presented in Figure 3.9 indicates that the noise floor in the vicinity of the 1600 Hz peak is approximately 10,000 times lower than the signal. This view of the FFT also revealed that there was very little energy present in the signal sidebands following the FFT process, indicating that no deviation from the 1600 Hz signal was detected by the microphone.

3.4 Chirp Response with Resonator

After the accuracy and repeatability of the resonator signal detection had been confirmed, the combined frequency response curve with the speaker and microphone *in situ* had to be analysed. The method used to test the frequency response in the resonator matched the process described in section 3.2 – record the audio signal produced by a chirp ascending from 500 Hz to 2500 Hz over a period of 20 seconds.

There were no further issues discovered during this round of tests. The FFT signal

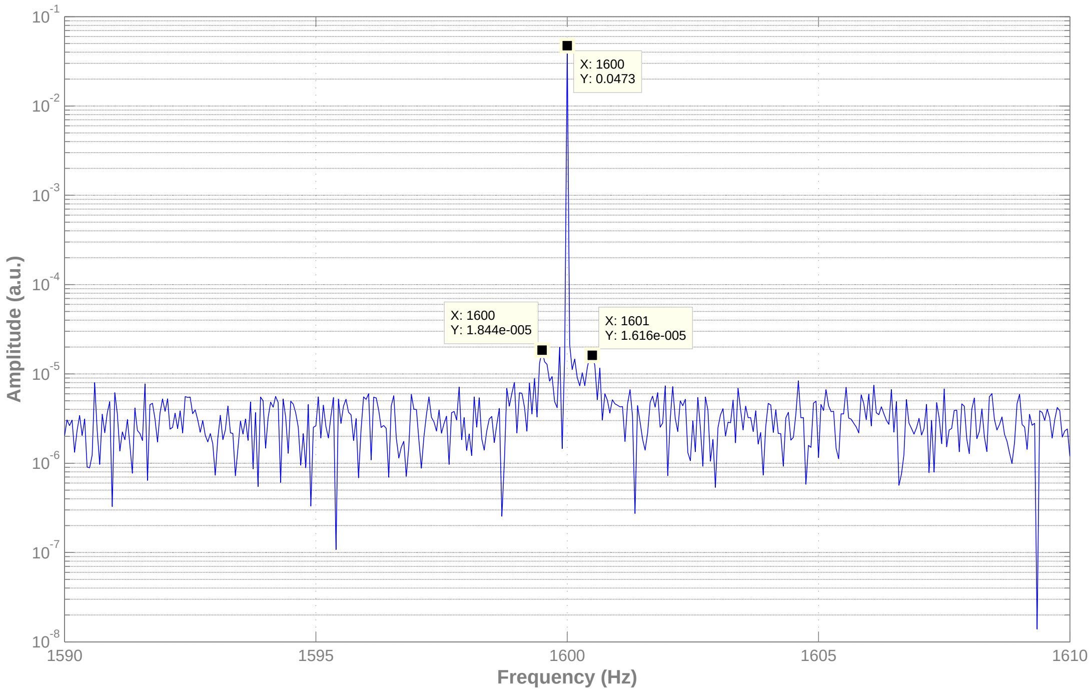

Figure 3.9: Magnified section of 1600 Hz resonator FFT, 1590 Hz to 1610 Hz

averaged over five consecutive chirps is shown in Figure 3.10.

Two notable differences between the frequency response with all components fitted to the prototype (Figure 3.10) and the combined response with the microphone removed from the resonator (Figure 3.7) are the lower bandwidth of the signal at a given frequency in the resonator, and the higher overall magnitude of the resonator signal.

Figure 3.11 is a comparative plot of the frequency response curves with the microphone installed in, and removed from, the resonator. Both signals have been filtered using a 1000-sample running average, and the signal with the microphone removed from the resonator has been normalised to the level of the resonator signal.

Although the shape of the two curves closely correspond, there are distinct peaks in the resonator chirp signal at 1600 Hz and 1850 Hz, followed by troughs at 1650 Hz and 2050 Hz. It is tempting to attribute the peak at 1600 Hz to the designed resonant frequency, but this claim is dubious at best.

Although the initial theoretical design was for a prototype resonant at 1600 Hz, there are fundamental differences between the open pipe resonator modelled with Equation 2.1 and the practical realisation of the cell. In the prototype, the pipe diameter is twice

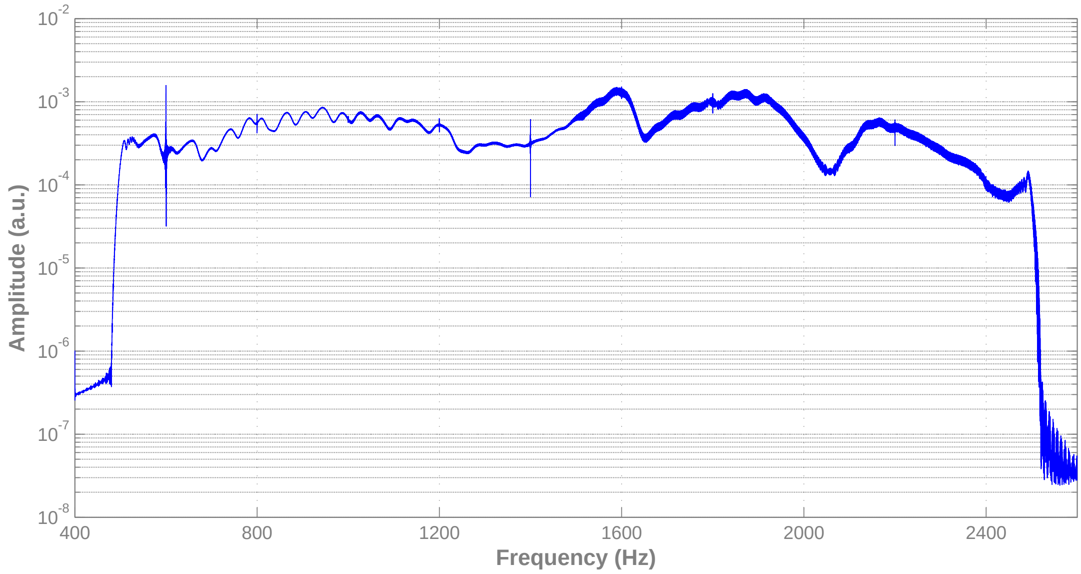

Figure 3.10: Combined microphone and speaker frequency response curve with resonator

that which was first proposed; the socket for the speaker elongates the pipe; the socket changes the pipe diameter; and the microphone is centred in the straight pipe but may not be located in the optimal position. An equation could not be found to neatly model the behaviour of the prototype as the divergence from the classical resonator models is so great. Measurement of the actual response was therefore the most conclusive method of determining the resonant frequency of the resonator tube; the resonant frequency of 1600 Hz is purely coincidental. The measured resonant peak centred at 1600 hertz is broad and shallow, and consequently small frequency movements in the region of the peak will not cause large changes in amplitude. The absence of a single large resonant response from the resonator also made

3.5 Frequency Tracking Response with Resonator

Following the successful completion of the preliminary testing, the tracking algorithm developed in section 2.2.3 could now be applied to data from the physical model. Similarly to the software simulations, two variable frequency audio files were created to test the response of the algorithm with a signal recorded by the resonator.

The first variable frequency source was a piecewise curve composed of three segments: a constant 1600 Hz sine wave, a linear chirp rising from 1600 Hz to 1630 Hz over a period of two seconds, and finally a constant 1630 Hz sine wave. The audio signal

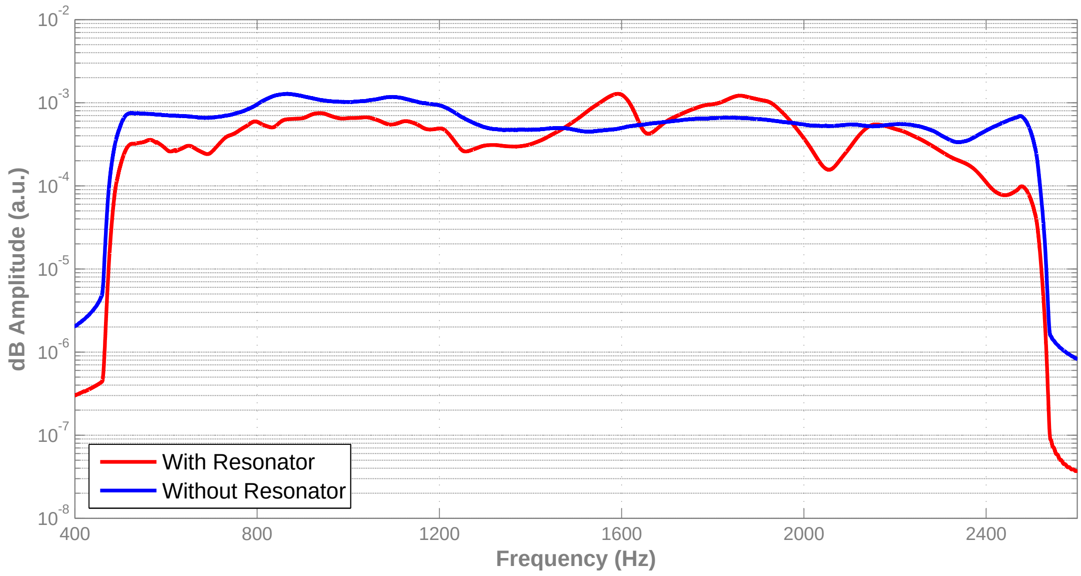

Figure 3.11: Frequency response curves with microphone in and out of resonator

was captured and pre-processed with a 1500 Hz to 1700 Hz bandpass filter to remove out-of-band components from the signal.

The filtered audio signal was subsequently fed into the algorithm, which broke the audio into small, overlapping windows, ran an FFT for each window, and determined the maximum frequency in each FFT. Windows sizes of 11025, 8820, 4410, and 3675 samples were used, with overlaps of 0% for the rectangular window and 10%, 25%, 50% and 90% for the Hamming window. A 1 Hz resolution of the signal was initially used to minimise execution time whilst testing and optimisation was undertaken.

The frequency vs. time plots in Figure 3.12 represent the highest quality resonant frequency tracking curves achieved with the window sizes and overlaps stated above. The results did not fit the known frequency change curve to the same extent that had been possible with the simulation.

The software simulation phase had used Hamming and rectangular windows, and as the resultant frequency tracking was satisfactory, it had not been necessary to test additional window styles. Given the poor outcome of the the first frequency tracking using the resonator, prototype testing extended the available range to include Hann and Kaiser windows. The shapes of the four selected windows, shown in Figure 3.13, are designed to attenuate the signal by different amounts at the centre and edges of the frames, giving different 'mixtures' between previous and current samples when

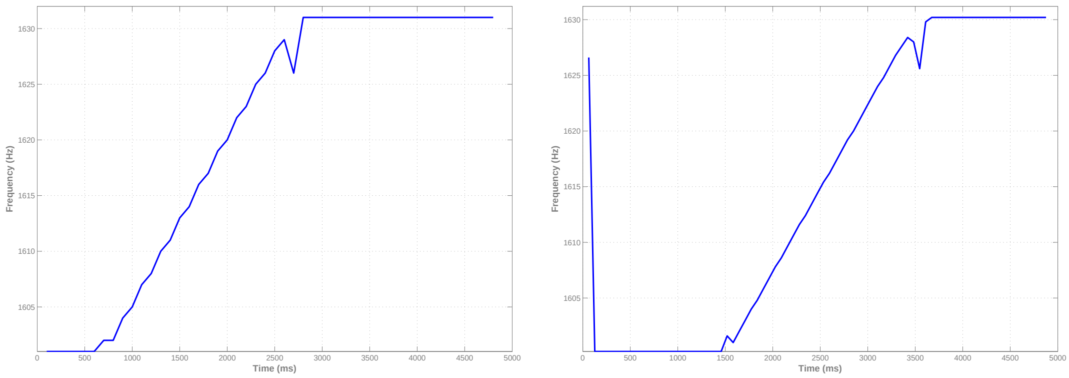

(a) Rectangular window, 0% overlap (b) Hamming window, 50% overlap

Figure 3.12: Frequency change tracking with window size of 8820 samples

overlapped.

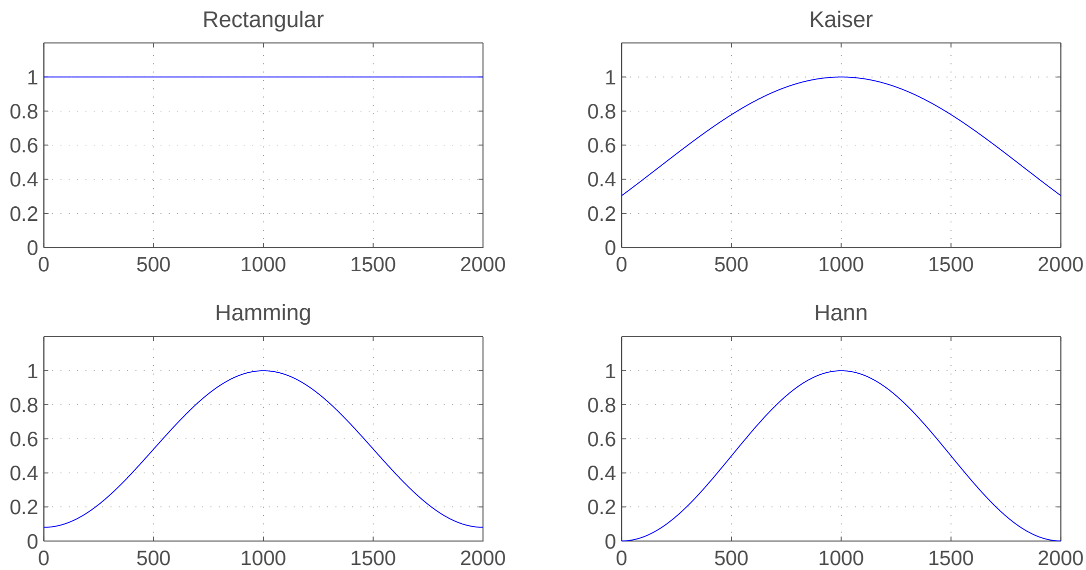

Figure 3.13: Window overlap shapes

Testing recommenced using all four window styles. The frequency tracking algorithm was presented with the same audio signal vector multiple times with all combinations of window styles, sample sizes and sample overlaps. Analysis of the results focused on the time taken to process the sample and the accuracy of the signal tracking. The processing time needed to be less than the length of the audio signal to ensure that it could be processed in real time. The signal accuracy was more difficult to quantify and evaluate. Taking the mean square difference between the actual and measured signal frequencies resulted in a robust method of comparing accuracy between measurements, but there were limitations to this technique. With low frequency resolution (1 Hz) and large window sizes, identical quality results were achieved by many windows. More differentiation was achieved when smaller window sample sizes were used, but the result was the same in each case: the 'best' combinations in each case performed poorly. Significant excursions from the actual signal were readily apparent on the plots, most notably at the points corresponding to sudden changes in frequency.

The signal artefacts were caused by a combination of mismatched overlaps between the windows, causing overlapping signals to be slightly out of phase, and through an unfortunate coincidence of all selected window sizes resulting in the piecewise curve segments occurring at the window edges. Some distortion of the audio signal at the segment joins was audible when the sound was played back through normal speakers, and this was expected to be replicated in the analysis of the recorded signal.

The extent of the problem is illustrated in Figure 3.14. A change in the window overlap of 10 samples is shown to change the tracked frequency by 7 Hz. Further testing of the same signal and smaller steps in window overlap sizes proved that the change between the two curves occurred with a step change of 1 sample, from 1066 to 1067 samples. The true figure at this point is midway between the two values, at 1630 Hz.

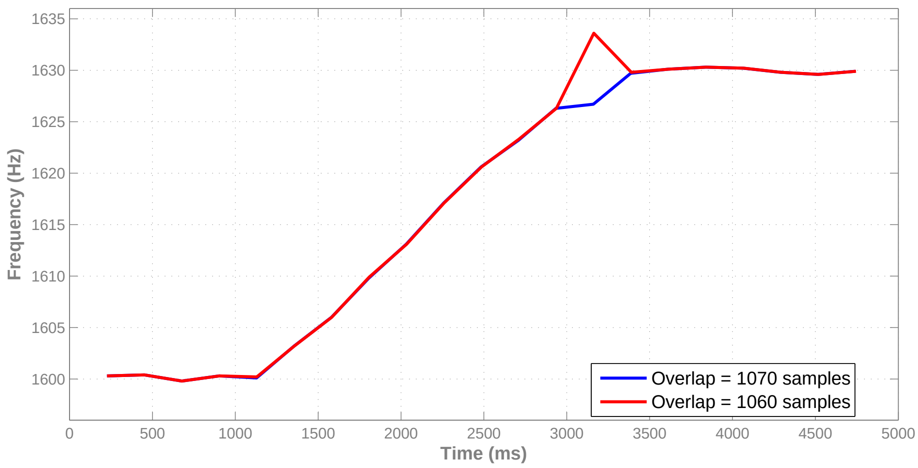

Figure 3.14: Hann window with 11025 samples and overlap of 1060 and 1070 samples

The sensitivity of the result to window size and the number of overlapping samples was unexpected and unwelcome. Further testing was performed with the same audio signal using arbitrary window sizes and number of samples in overlapping frames. The results are tabulated in Table 3.1, and illustrate the extent to which the accuracy of the signal tracking algorithm is dependent on the overlap.

Virtually any window size can be used to determine the change in frequency. Large

Table 3.1: Speed and accuracy of different windows styles, frame sizes, and frame overlaps. Indicated qualities are **P**oor, **F**air, **G**ood, and **E**xcellent.

Number of Samples		Window Style							
		Rectangular		Kaiser		Hann		Hamming	
Window	Overlap	Time	Quality	Time	Quality	Time	Quality	Time	Quality
11025	0	0.64	F	-	-	-	-	-	-
	1103	-	-	0.63	F	0.63	F	0.61	F
	2205	-	-	0.61	F	0.59	F	0.61	F
	2400	-	-	0.6	**E**	0.59	**E**	0.61	**E**
	5513	-	-	0.88	G	0.87	G	0.86	G
	8269	-	-	1.54	G	1.51	G	1.47	G
	9923	-	-	3.33	G	3.33	F	3.38	G
8820	0	0.56	F	-	-	-	-	-	-
	882	-	-	0.55	P	0.53	F	0.55	F
	1764	-	-	0.62	F	0.57	P	0.59	P
	2950	-	-	0.69	**E**	0.71	**E**	0.66	**E**
	4410	-	-	0.91	F	0.87	F	0.89	F
	6615	-	-	1.55	F	1.56	F	1.57	F
	7938	-	-	3.59	P	3.62	P	3.71	P
9350	600	-	-	0.53	F	0.53	F	0.55	F
	800	-	-	0.54	**E**	0.52	G	0.53	G
	900	-	-	0.59	**E**	0.57	**E**	0.58	**E**
	1100	-	-	0.58	P	0.57	P	0.57	P
4410	0	0.67	P	-	-	-	-	-	-
	441	-	-	0.75	P	0.73	P	0.73	P
	882	-	-	0.86	P	0.81	P	0.84	P
	2205	-	-	1.25	P	1.25	P	1.24	P
	3969	-	-	6.3	P	5.86	P	5.86	P
3675	0	0.79	P						
	368	-	-	0.85	P	0.86	P	0.85	P
	735	-	-	0.94	P	0.93	P	0.94	P
	1838	-	-	1.45	P	1.46	P	1.46	P
	3308	-	-	6.91	P	6.78	P	6.92	P

windows and small overlaps are quick to process but result in coarser update rate for frequency changes, and a larger frequency step size. Conversely, small windows and large overlaps take longer to analyse and give more granular results, but the increased processing time does not come with a commensurate increase in accuracy. Small windows contain too few waveform cycles for the FFT to calculate the frequencies to any great degree of certainty. The values in Table 3.1 indicate that large windows and overlaps of an arbitrary size give the best frequency tracking accuracy, as illustrated by plots of two of the best-performed combinations of window size and overlap in Figure 3.15.

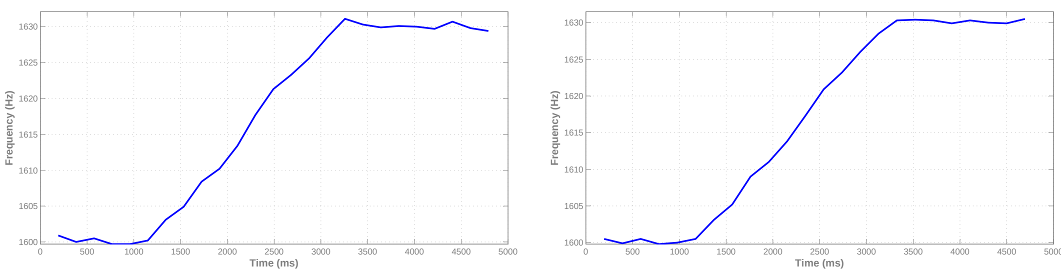

(a) Kaiser, 9350 samples, 9.6% overlap

(b) Hann, 11025 samples, 21.8% overlap

Figure 3.15: Frequency tracking algorithm - most accurate results with original algorithm

This outcome is problematic. Arbitrary sample overlap sizes are inconsequential during testing, as the signal can be iteratively processed with small changes in overlapping samples until the optimal result is achieved. This implies knowledge of the real sample frequency at all times, as the comparison to evolve the window sizes is predicated on the error between measured and actual values. In a scenario where the real frequency is unknown, as can be expected in measurements from working photoacoustic resonators, this approach will not work. Changing the sample overlap size will result in different frequencies being selected from the FFT, but there is not a known signal against which to compare it. There is no way to correctly distinguish between an analysis point that is tracking the frequency, and one which is affected by an incorrect choice of window size.

In light of the issues described above, the algorithm had to be modified to remove arbitrary dependencies. As the problem was evidenced most clearly at the joins between frames, the modification to the algorithm attempted to alleviate this issue.

Initially, the signal was buffered into smaller segments corresponding to a period of time, such as 500 ms. The top and bottom 10% of values were discarded, and the FFT processed the middle 80% of values. This approach was not successful, and suffered from the same inconsistencies between the maximum frequency values in consecutive frames.

With the failure of this approach, it was apparent that the issues were not caused by the frame edges *per se*, but were instead related to partial waveforms present at the extreme ends of the frames, which were sufficient to disrupt the FFT calculation. Consequently, the algorithm was modified to fill the start of each segment with zeroes until the first positive-going zero crossing was encountered, and to fill the end of each frame with zeros after the last negative-going zero crossing was found. After processing, each frame would therefore be left with only whole cycles of the waveform. This method was much more successful; resultant plots for update times of 500 ms and 200 ms are displayed in Figure 3.16.

The 500 ms update time curve in Figure 3.16 tracks the actual frequency to a high degree of accuracy. The frequency tracking curve with a 200 ms update time is not as smooth; each 200 ms window contains approximately 320 full cycles of the waveform, which was just sufficient for the FFT to process accurately. Smaller window sizes of 150 ms (240 samples) were unable to reproduce an accurate tracking curve.

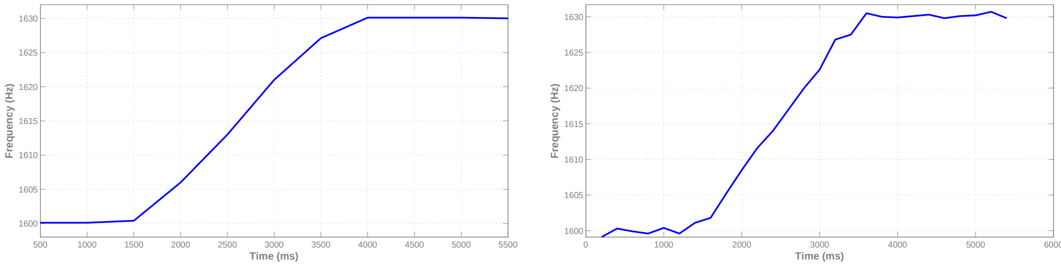

(a) 500 ms update time (b) 200 ms update time

Figure 3.16: Modified frequency tracking algorithm - three segments, partial waveforms discarded

The whole-waveform method of analysis was also faster than windowing the samples after buffering. With a resolution of 0.1 Hz, the curve with a 500 ms update time took 250 ms to process, and the 200 ms update time curve required only 350 ms to process. These compare favourably with the 640 ms and 560 ms processing times needed for the coarser 1 Hz signals documented in Table 3.1.

Following the successful application of the modified algorithm, the second of the two variable frequency audio signals was tested. The second audio file was constructed from five segments; a fixed 1600 Hz sine wave to start, three 15 Hz per second linear chirp segments rising to 1615 Hz, falling to 1585 Hz, and rising again to 1600 Hz, and lastly a constant 1600 Hz sine wave to finish.

The modified algorithm was able to track the frequency change of the five-segment curve without difficulty. The resultant plots are displayed in Figure 3.17.

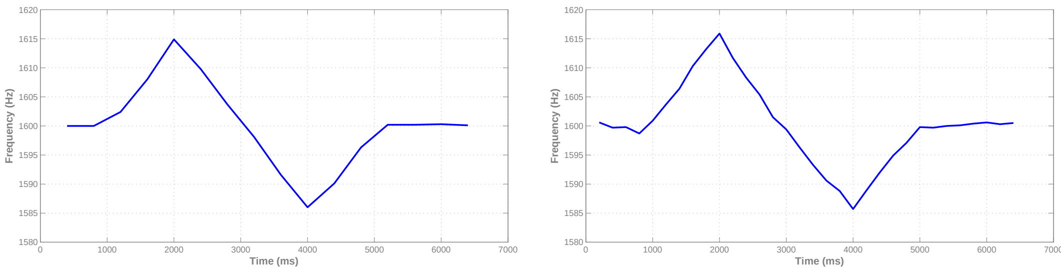

(a) 400 ms update time (b) 200 ms update time

Figure 3.17: Modified frequency tracking algorithm - five segments, partial waveforms discarded

The five-segment audio waveform was longer than the three-segment, clocking in at 7 seconds. The first half-second of the waveforms was discarded, as the microphone circuit added noise to the signal as it started capturing the audio. The 6.5 seconds of audio required 230 ms to process with 400 ms between frequency updates, and needed 490 ms to produce the 200 ms update time curve.

The modified algorithm is able to process the audio signals faster than real-time; this leaves open the possibility of further improvement to the algorithm by interpolating the frequency tracking signal using multiple data sets that are slightly offset.

3.6 Measuring Cell Resonant Frequency

The final step of the testing process involved the application of the frequency tracking algorithm to determining the resonant frequency of the cell across a range of temperatures. As discussed in section 2.1 and presented in Table 2.1, if the air temperature inside the resonator is decreased, the resonant frequency of the cell will decrease. Conversely, an increase in temperature within the resonator cavity will result in a higher resonant frequency.

The tracking algorithm had been developed to a point where it could accurately and consistently track the peak frequency over time. To translate the peak frequency tracking to resonant frequency tracking, an audio signal encompassing a broad range around the resonant frequency was required. An audio waveform spanning 1580 Hz to 1620 Hz with 5 Hz steps was constructed and played through the speaker. The expectation was that a single frequency would dominate and the frequency tracking would show a flat line. This assumption was based on the resonator temperature remaining static for the few seconds the measurement was being completed, and the speaker being the only source of acoustic energy for the microphone.

The actual result, displayed on a plot with a 200 ms update time in Figure 3.18, was considerably different. The frequency fluctuations were not overly dramatic, but the fact that they existed at all was concerning.

After some investigation, an FFT of the audio signal recorded by the microphone revealed that each of the 5 Hz steps was being played and recorded separately. Using different time bases, the sawtooth signal as the speaker jumped between frequencies became apparent. Using 200 ms and 500 ms update times from the frequency tracking

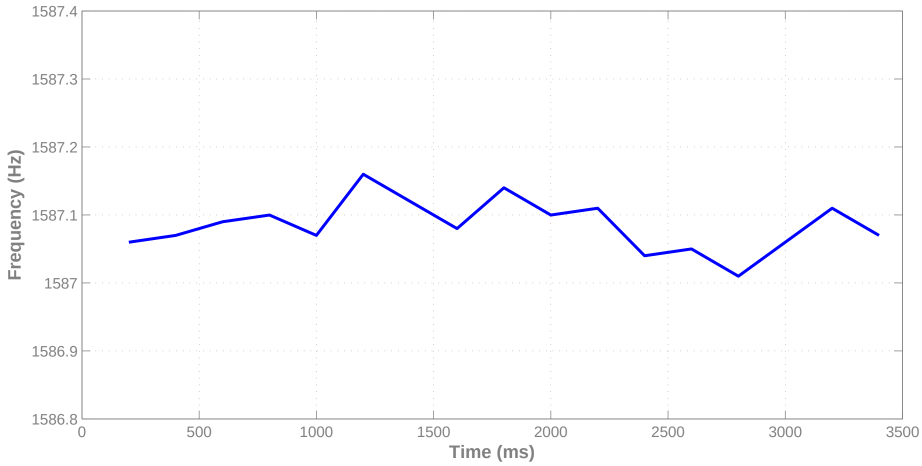

Figure 3.18: Resonant frequency tracking with 40 Hz window and 5 Hz steps

algorithm had initially masked the problem. The FFT of the audio waveform played over the speaker indicated that each discrete frequency had an identical amount of energy, but the recorded audio displayed a slight bias toward the lower end of the frequency spectrum.

A new audio file with a narrower frequency range of 1590 Hz to 1610 Hz and smaller step size of 5 Hz was created. The resultant signal from the frequency tracking algorithm was little changed, and the FFT of the recorded audio signal, shown in Figure 3.19, also indicated that the discrete frequencies were being picked up.

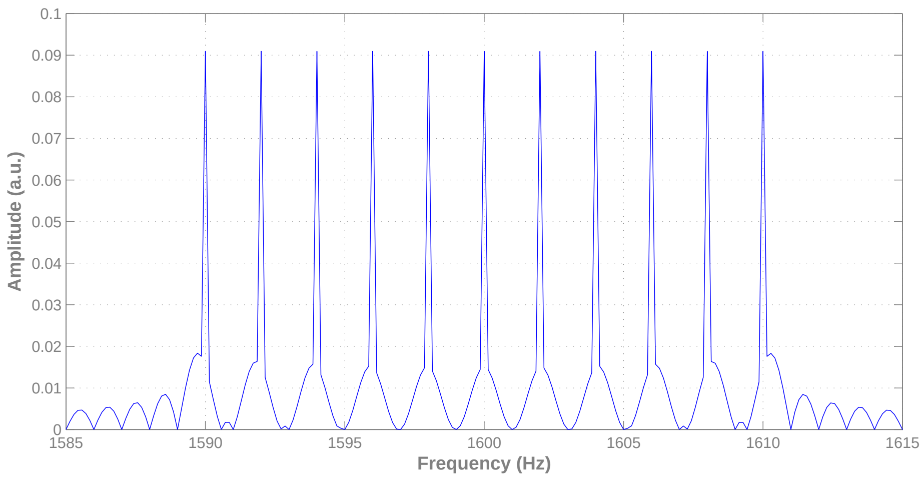

Figure 3.19: FFT of 20 Hz window with 2 Hz steps showing separation between frequencies

It had become apparent that resonant frequency tracking would not work with the developed algorithm unless an audio signal could deliver an equal amount of power across the frequency spectrum. The gaps in the frequency bands were being detected by the FFT and the algorithm was tracking the discrete frequencies rather than a single, dominant, resonant frequency. The final attempt to overcome the problem involved closing the gap between frequencies to a very small level.

Another audio file was created, again spanning the range 1590 Hz to 1610 Hz, but with a much smaller step size of 0.05 Hz. The recorded audio was processed by the algorithm, which once more exhibited a sawtooth pattern when processed with a 400 ms sample rate. The tracked signal oscillated neatly between 1590 Hz and 1610 Hz, and the reason for the definite pattern emerged when the FFT of Figure 3.20 was viewed. Equal amplitudes at each 0.05 Hz had resulted not in a signal with energy distributed equally across the spectrum, but instead in a curve where the energy was concentrated at the two frequency extremes.

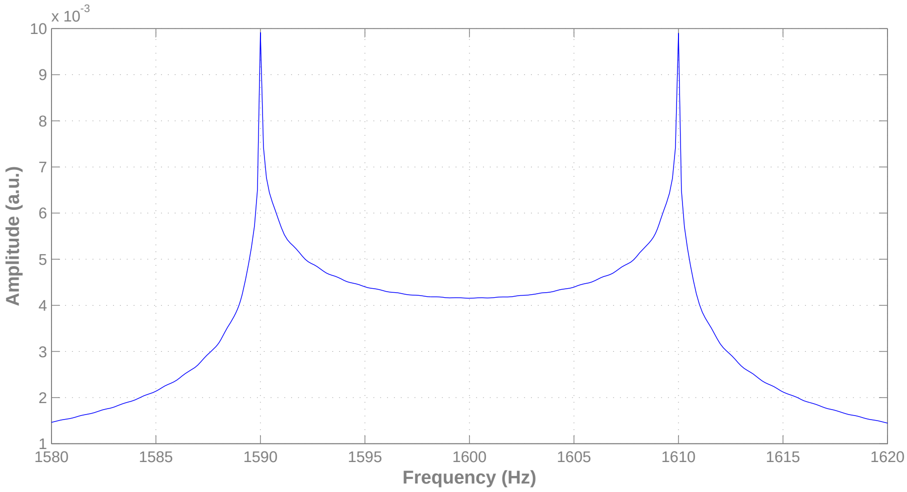

Figure 3.20: FFT of 20 Hz window with 0.05 Hz steps showing unequal energy distribution across frequencies

In the ensuing period, further investigations were conducted in an effort to find a solution that would enable the experiment to continue. Different methods of producing chirp signals were tested, other MATLAB audio functions were examined, and many promising user functions from the MATLAB File Exchange were checked, all to no avail.

The final piece of the resonant frequency tracking algorithm would require a fundamentally different approach, entailing a significant amount of rework in the hope of achieving a successful outcome. Due to time constraints, it was not possible to develop and test alternative methods to meet all the project goals, and consequently the experimental phase of the project was drawn to a close.

Chapter 4

Conclusion and Further Work

Photoacoustic spectroscopy has found widespread adoption and acceptance in research and industrial facilities across the world. The key advantages photoacoustic resonator cells enjoy over other analysers are their excellent sensitivity and selectivity. Photoacoustic cells can measure the concentration of constituent gases down to a level of parts per trillion, and with careful selection of laser wavelengths, allow multiple components to be analysed simultaneously.

Photoacoustic technology has improved and matured over past four decades, and the majority of operational issues have been resolved during that period. One significant outstanding problem is the sensitivity of the resonant frequency of the acoustic cell to variations in ambient conditions, and in particular, temperature changes. In laboratory environments, sample handling systems can control the temperature of the gas entering the cell. Where high sensitivity is not required, low-Q cells are used to minimise the effect of temperature drift. Other compensation arrangements include additional circuitry and multiple cells to correct for temperature changes. These approaches prevent temperature variability rather than adapting to changing conditions.

If the resonant frequency of a photoacoustic cell is able to be detected in real time, the frequency of the laser can be modulated to match the resonant frequency. This would ensure that the relationship between the amplitude of the acoustic signal and the concentration of gas is independent of the resonant frequency, and would allow the generated acoustic signal to be maximised regardless of temperature.

The primary focus of this research was directed toward determination the resonant frequency of a photoacoustic cell in real time and under varying ambient conditions. Five goals were proposed in the project specification to guide the research toward the achievement of this goal. The first two related to gaining an understanding of the history, development, construction, and use of photoacoustic resonators, and are addressed in chapter 1. The three remaining goals pertained to improving resonant frequency tracking: software simulation of algorithms, construction a resonator cell to test the practicality and performance of the algorithm, and comparison of theoretical and measured results.

Published research on photoacoustic resonators discusses modelling the response of different cell types, and all authors caution that an accurate determination of the resonant frequency can only be achieved through measurement. Following the direction taken by Suchenek (2014), the preferred solution involved playing a signal containing superimposed frequencies into the resonator, recording the response, and analysing the signal in real time to establish deviation of the resonant frequency.

Constraints on the design of the prototype, including buildability, safety considerations, and availability of electronic components, were taken into consideration when developing the software models. Consequently, a simplified open-tube photoacoustic resonator was used to develop the basic equations relating resonator dimensions, temperature, and the speed of sound. This formed the basis for development of the frequency tracking function and and computer simulation code.

The frequency tracking was developed using FFTs due to their familiarity and ease of application. Amongst a host of new concepts, chirp signals and FFT windowing and overlapping were most critical to the development of the frequency tracking algorithm, and had to be studied and understood prior to their use in the code. The simulated performance of the algorithm was tested using clean and noisy sine waves, simple rising tones, and tones that both increased and decreased in frequency. In all cases, the algorithm was able to distinguish the dominant frequency and accurately plot a curve of the change in frequency over time.

Without a workshop and specialised tooling, construction of the prototype was a flawed enterprise from the start. It was not able to be constructed as originally envisaged as all components were larger than desired. Even such a simple device was time-consuming to make, and anything more complex would have been too difficult to manufacture with the available tools. One enjoyable aspect of the build was the first use of AutoCAD 3D to create the dimensional drawing of the prototype. The prototype was marginally acceptable for testing purposes, but was far from an ideal model.

Once testing commenced, the resonant frequency of the prototype was clearly visible in the graphs comparing the frequency response curves of the speaker and microphone both in and out of the resonator. Substantial signal amplification could be expected when operating in this region. In light of the compromised design, the peak resonant frequency occurring at the design point was purely coincidental, but was nonetheless gratifying.

The frequency tracking algorithm performed much more poorly in the physical prototype than in the simulations. Distortions in the frequency tracking plots remained obstinately immovable, necessitating changes to the algorithm. This initially involved using different window styles in the in FFTs, and when these failed to make an impact, the theory behind windowing was examined more closely. The over-sensitivity to the number of samples by which the windows overlapped could not be avoided, and precluded the use of the original algorithm to test the prototype. More rigorous testing of the simulation code would probably have revealed this weakness at an earlier stage, avoiding the need to change the algorithm whilst the prototype was being tested.

The realisation that partial waveforms at the beginning and end of each frame were the cause of the signal discontinuities led to the creation of the novel technique of zeroing the audio frames prior to the first positive-going waveform and after the last negative-going waveform. Ensuring that the FFT always able to operate on complete waveforms greatly enhanced the robustness of the algorithm. Following the modifications, both the speed and quality of the results exceeded those that had been achieved with the original algorithm.

Further improvement of the final algorithm is possible. By removing a limited number of samples from the front of the recorded audio vector and re-processing the remaining sample, successive results can be used to interpolate the original results. This technique would allow much finer frequency precision to be achieved.

The final frequency tracking test was a failure. A wide swathe of frequencies was to be tested simultaneously by means of a broad-spectrum chirp. The resonant frequency would have the greatest amplitude in the measured signal, and this could be identified and tracked. However, it was not possible to generate a sufficiently flat audio signal across the required range, resulting in frequencies at the extreme ends of the chirp signal dominating in the recorded signal. Although this does not lessen the results achieved throughout the remainder of the experimental phase, it precludes this technique from being used in a practical application.

If this research were to be undertaken again, several changes to the methodology would be seriously considered. Relying on every process to work as designed was a losing strategy, as one failure in one routine rendered the entire resonant frequency tracking arrangement unworkable. Redundancy is good, although difficult to achieve in iterative designs such as this. More upfront research does not necessarily translate to better outcomes, as flaws in one approach to a problem may not manifest themselves until much later in the development process.

Concurrently developing multiple solutions to a problem is a sound approach to solving an intricate or difficult problem. In this case, having several alternatives may have avoided the unsuccessful conclusion through the ability to resume testing using another method. However, the research process is arduous to document, and a second solution, or even a comparative analysis of techniques, requires a greater commitment of time and resources to achieve. Notwithstanding the additional effort required, if this research were to be repeated, a second solution to the primary problem of resonant frequency tracking would be fully developed as an adjunct to the preferred method.

On a personal level, valuable knowledge was acquired with respect to FFTs, windowing functions, signal detection, signal processing, 3D modelling, and photoacoustic spectroscopy during execution of the project.

Although the project was ultimately unsuccessful in finding a solution to resonant frequency tracking in photoacoustic cells, all five research goals were achieved. The frequency tracking algorithms developed are useful and exhibit reasonable performance, but have a limited audience due to their specialised nature.

References

Angeli, G. Z., Bozóki, Z., Miklós, A., Lörincz, A., Thöny, A. & Sigrist, M. W. (1991), 'Design and characterization of a windowless resonant photoacoustic chamber equipped with resonance locking circuitry', *Review of Scientific Instruments* **62**(3), 810. http://ezproxy.usq.edu.au/login?url=http://search.ebscohost.com/login.aspx?direct=true&db=a9h&AN=9785129&site=ehost-live.

Bartlome, R., Kaučikas, M. & Sigrist, M. (2009), 'Modulated resonant versus pulsed resonant photoacoustics in trace gas detection', *Applied Physics B* **96**(2-3), 561–566. http://dx.doi.org/10.1007/s00340-009-3572-2.

Bell, A. G. (1880), 'On the production and reproduction of sound by light', *American Journal of Science* **20**(118), 294–302. http://www.ajsonline.org/content/s3-20/118/305.full.pdf+html.

Berg, D., VanderNoot, V., Barradas, R. & Lai, E. (1994), 'In-situ photoacoustic investigation of thallium underpotential deposition on polycrystalline copper electrodes', *Journal of Electroanalytical Chemistry* **369**(1-2), 33 – 37. http://www.sciencedirect.com/science/article/pii/0022072894870802.

Besson, J.-P., Schilt, S. & Thévenaz, L. (2006), 'Sub-ppm multi-gas photoacoustic sensor', *Spectrochimica Acta Part A: Molecular and Biomolecular Spectroscopy* **63**(5), 899 – 904.

Bialkowski, S. (1996), *Photothermal Spectroscopy Methods for Chemical Analysis*, Chemical Analysis: A Series of Monographs on Analytical Chemistry and Its Applications, John Wiley and Sons.

Bijnen, F. G. C., Reuss, J. & Harren, F. J. M. (1996), 'Geometrical optimization of a longitudinal resonant photoacoustic cell for sensitive and fast trace gas detection', *Review of Scientific Instruments* **67**(8), 2914–2923. http://scitation.aip.org/content/aip/journal/rsi/67/8/10.1063/1.1147072.

Bonno, B., Laporte, J. L. & D'Leon, R. T. (2005), 'Measurement of thermal properties of gases using an open photoacoustic cell as a sensor', *Review of Scientific Instruments* **76**(9), 096104. http://ezproxy.usq.edu.au/login?url=http://search.ebscohost.com/login.aspx?direct=true&db=iih&AN=18415526&site=ehost-live.

Borowski, T. & Starecki, T. (2008), 'Photoacoustic signal generation based on self-oscillation method', *The European Physical Journal Special Topics* **153**(1), 439–441. http://dx.doi.org/10.1140/epjst/e2008-00480-x.

Corbin, R. (1992), 'Photoacoustic detection and tracking apparatus'. https://www.google.com/patents/US5129255.

Dickherber, A. (2008), Design, fabrication, and testing of an acoustic resonator-based biosensor for the detection of cancer biomarkers, PhD thesis, Georgia Institute of Technology.

Electus Distribution (2014), 'Standard microphone insert'. http://www.electusdistribution.com.au/products_uploaded/AM4010_datasheet.pdf.

Elia, A., Lugarà, P. M., Di Franco, C. & Spagnolo, V. (2009), 'Photoacoustic techniques for trace gas sensing based on semiconductor laser sources', *Sensors* **9**(12), 9616–9628. http://www.mdpi.com/1424-8220/9/12/9616.

Google (2013), 'Google Ngram viewer'. https://books.google.com/ngrams/graph?content=CO2+laser%2Cphotoacoustic&case_insensitive=on&year_start=1950&year_end=2008&corpus=15&smoothing=7&share=&direct_url=t4%3B%2CCO2%20laser%3B%2Cc0%3B%2Cs0%3B%3BCO2%20laser%3B%2Cc0%3B%3BCO2%20Laser%3B%2Cc0%3B.t4%3B%2Cphotoacoustic%3B%2Cc0%3B%2Cs0%3B%3Bphotoacoustic%3B%2Cc0%3B%3BPhotoacoustic%3B%2Cc0%3B%3BPHOTOACOUSTIC%3B%2Cc0.

Holthoff, E., Bender, J., Pellegrino, P. & Fisher, A. (2010), 'Quantum cascade laser-based photoacoustic spectroscopy for trace vapor detection and molecular discrimination', *Sensors* **10**(3), 1986–2002. http://www.mdpi.com/1424-8220/10/3/1986.

Jaycar Electronics (2014*a*), 'Mini microphone insert - 6 x 3.5mm'. `http://www.jaycar.com.au/productView.asp?ID=AM4008`.

Jaycar Electronics (2014*b*), 'Shielded 1" 1w 8-ohm full range speaker'. `http://www.jaycar.com.au/productView.asp?ID=AS3030`.

Kalkman, J. & van Kesteren, H. W. (2008), 'Relaxation effects and high sensitivity photoacoustic detection of NO_2 with a blue laser diode', *Applied Physics B: Lasers & Optics* **90**(2), 197 – 200. `http://ezproxy.usq.edu.au/login?url=http://search.ebscohost.com/login.aspx?direct=true&db=a9h&AN=28857714&site=ehost-live`.

Kästle, R. & Sigrist, M. W. (1996), 'Temperature-dependent photoacoustic spectroscopy with a Helmholtz resonator', *Applied Physics B: Lasers & Optics* **63**(4), 389. `http://ezproxy.usq.edu.au/login?url=http://search.ebscohost.com/login.aspx?direct=true&db=a9h&AN=8825583&site=ehost-live`.

Kinsler, L. E., Frey, A. R., Coppens, A. B., & Sanders, J. V. (2000), *Fundamentals of acoustics*, 4th edn, Wiley.

Koskinen, V., Fonsen, J., Kauppinen, J. & Kauppinen, I. (2006), 'Extremely sensitive trace gas analysis with modern photoacoustic spectroscopy', *Vibrational Spectroscopy* **42**(2), 239 – 242. `http://www.sciencedirect.com/science/article/pii/S0924203106001202`.

Kosterev, A. A., Tittel, F. K., Serebryakov, D. V., Malinovsky, A. L. & Morozov, I. V. (2005), 'Applications of quartz tuning forks in spectroscopic gas sensing', *Review of Scientific Instruments* **76**(4), 043105. `http://ezproxy.usq.edu.au/login?url=http://search.ebscohost.com/login.aspx?direct=true&db=a9h&AN=16702397&site=ehost-live`.

Kreuzer, L. B. (1971), 'Ultralow gas concentration infrared absorption spectroscopy', *Journal of Applied Physics* **42**(7), 2934–2943. `http://scitation.aip.org/content/aip/journal/jap/42/7/10.1063/1.1660651`.

Leytner, S. & Hupp, J. T. (2000), 'Charge transfer at nanocrystalline metal oxide semiconductor/solution interfaces studied by photoacoustic spectroscopy', `http://www.photobiology.com/photoiupac2000/leytner/index.htm`.

Mallidi, S., Larson, T., Tam, J., Joshi, P. P., Karpiouk, A., Sokolov, K. & Emelianov, S. (2009), 'Multiwavelength photoacoustic imaging and plasmon resonance coupling of gold nanoparticles for selective detection of cancer', *Nano Letters* **9**(8), 2825–2831. http://pubs.acs.org/doi/abs/10.1021/nl802929u.

Mattiello, M. (2008), Gas Trace Measurement by Photoacoustic spectroscopy using Helmholtz resonator-based sensors, PhD thesis, École Polytechnique Fédérale de Lausanne.

Meyer, P. L. & Sigrist, M. W. (1990), 'Atmospheric pollution monitoring using CO_2 laser photoacoustic spectroscopy and other techniques', *Review of Scientific Instruments* **61**(7), 1779–1807. http://scitation.aip.org/content/aip/journal/rsi/61/7/10.1063/1.1141097.

Miklós, A., Hess, P. & Bozóki, Z. (2001), 'Application of acoustic resonators in photoacoustic trace gas analysis and metrology', *Review of Scientific Instruments* **72**(4), 1937. http://ezproxy.usq.edu.au/login?url=http://search.ebscohost.com/login.aspx?direct=true&db=iih&AN=4716644&site=ehost-live.

National Instruments (2009), 'Performing an STFT versus time (sound and vibration measurement suite)'. http://zone.ni.com/reference/en-XX/help/372416A-01/svtconcepts/perform_stft_time/.

Pilgrim, J., Bomse, D. & Silver, J. (2003*a*), 'Acoustic resonance frequency locked photoacoustic spectrometer'. http://www.google.com/patents/US6618148.

Pilgrim, J., Bomse, D. & Silver, J. (2003*b*), 'Acoustic resonance phase locked photoacoustic spectrometer'. http://www.google.com/patents/US6608683.

Rosencwaig, A. & Gersho, A. (1976), 'Theory of the photoacoustic effect with solids', *Journal of Applied Physics* **47**(1), 64–69. http://scitation.aip.org/content/aip/journal/jap/47/1/10.1063/1.322296.

Santiago, G., Slezak, V. & Peuriot, A. (2003), 'Resonant photoacoustic gas sensing by PC-based audio detection', *Applied Physics B: Lasers & Optics* **77**(4), 463 – 465. http://ezproxy.usq.edu.au/login?url=http://search.ebscohost.com/login.aspx?direct=true&db=a9h&AN=11535639&site=ehost-live.

Sorvajärvi, T., Manninen, A., Toivonen, J., Saarela, J. & Hernberg, R. (2009), 'Resonant photoacoustic cell for pulsed laser analysis of gases at high temperature', *Review of Scientific Instruments* **80**(12), 123103. http://ezproxy.usq.edu.au/login?url=http://search.ebscohost.com/login.aspx?direct=true&db=iih&AN=47244392&site=ehost-live.

Spagnolo, V., Patimisco, P., Borri, S., Scamarcio, G., Bernacki, B. E. & Kriesel, J. (2013), Part-per-trillion level detection of SF_6 using a single-mode fiber-coupled quantum cascade laser and a quartz enhanced photoacoustic sensor, *in* S. of Photo-Optical Instrumentation Engineers, ed., 'Proc. Quantum Sensing and Nanophotonic Devices X', Vol. 8631, Society of Photo-Optical Instrumentation Engineers. http://dx.doi.org/10.1117/12.2001638.

Starecki, T. (2008), 'Windowless open photoacoustic Helmholtz cell', *Acta Phys. Pol. A* **114**, A211–A216. przyrbwn.icm.edu.pl/APP/PDF/114/a114zA34.pdf.

Starecki, T. & Owczarek, T. (2007), Comparison of FFT and LMS applied to photoacoustic signal detection, *in* 'Photonics Applications in Astronomy, Communications, Industry, and High-Energy Physics Experiments 2007', Vol. 6937, pp. 693710–693710–7. http://dx.doi.org/10.1117/12.784664.

Suchenek, M. (2014), 'A novel method of evaluating the frequency response of a photoacoustic cell', *International Journal of Thermophysics* pp. 1–5. http://dx.doi.org/10.1007/s10765-014-1612-6.

Suchenek, M. & Starecki, T. (2011), 'Pulse measurements of the frequency response of a photoacoustic cell', *International Journal of Thermophysics* **32**(4), 893–900. http://dx.doi.org/10.1007/s10765-011-0955-5.

Szakáll, M., Varga, A., Pogány, A., Bozóki, Z. & Szabó, G. (2009), 'Novel resonance profiling and tracking method for photoacoustic measurements', *Applied Physics B* **94**(4), 691–698. http://dx.doi.org/10.1007/s00340-009-3391-5.

Tam, A. C. (1986), 'Applications of photoacoustic sensing techniques', *Rev. Mod. Phys.* **58**, 381–431. http://link.aps.org/doi/10.1103/RevModPhys.58.381.

The State of Queensland (Department of Education, Training and Employment) (2012), 'Risk management'. http://education.qld.gov.au/health/safety/managing/risk.html.

Timmer, B., Olthuis, W. & Berg, A. v. d. (2005), 'Ammonia sensors and their applications - a review', *Sensors and Actuators B: Chemical* **107**(2), 666–677. http://www.sciencedirect.com/science/article/pii/S0925400504008196.

Appendix A

Project Specification

ENG 4111/2 Research Project

Project Specification

For:	**David McLaughlin**
Topic:	Resonator Probe for Photoacoustic Measurement
Supervisors:	Dr. John Leis
Sponsorship:	Faculty of Health, Engineering & Sciences

Project Aim: The resonant frequency of the sound detected by a photoacoustic resonator is sensitive to ambient conditions such as the temperature and pressure of the sampled gas.

The goal of this project is to determine methods of identifying the resonant frequency of a sample under varying conditions. The focus will be on the speed and accuracy of detection of the resonant frequency, and the ability to track the resonant frequency as conditions change.

Program:

1. Research background information on photoacoustic resonator construction.
2. Research background information on frequency detection in photoacoustic resonators.
3. Implement software simulation of resonance tracking methods, based on mathematical models.
4. Design, construct, and test a photoacoustic resonator suitable for use in testing and simulation.
5. Compare the performance of the theoretical algorithms with the results from the prototype.

As time and resources permit:

1. Theoretically determine the performance of the resonance tracking algorithms using simulated variable ambient conditions.
2. Test the prototype under variable ambient conditions, and compare the resultant data against the theoretical performance.

Agreed:

Student Name:	David McLaughlin
Date:	2014-03-19
Supervisor Name:	Dr. John Leis
Date:	
Examiner:	Chris Snook
Date:	

Appendix B

Job Safety Analysis Forms

Two job safety analysis worksheets (JSAs) were prepared for use during the execution of this project. The JSAs risk-assessed the manufacture of the resonator from copper tube, and soldering the speaker and microphone cables.

The form used was adapted from a resource provided by the Queensland Government (The State of Queensland (Department of Education, Training and Employment) 2012).

Risk Assessment Template

Use this template to document a risk assessment to manage health and safety hazards and risks.
For more details on the risk management process refer to, *Managing Health and Safety Risks*.
Note: For risk assessments with curriculum activities refer to: *Managing Risks in School Curriculum Activities*.

Activity Description: **Manufacture open pipe resonator**	
Conducted by: **David McLaughlin**	Date: **03 Sept 2014**

Step 1: Identify the Hazards

Biological (e.g. hygiene, disease, infection)		
☐ Blood / Bodily fluid	☐ Virus / Disease	☐ Food handling
Other/Details:		
Chemicals Note: Refer to the label and Safety Data Sheet (SDS) for the classification and management of all chemicals.		
☒ Non-hazardous chemical(s)	☐ 'Hazardous' chemical (Refer to a completed hazardous chemical risk assessment)	
Name of chemical(s) / Details: Flux paste, Silastic		
Critical Incident – resulting in:		
☐ Lockdown	☐ Evacuation	☐ Disruption
Other/Details:		
Energy Systems – incident / issues involving:		
☐ Electricity (incl. Mains and Solar)	☐ LPG Gas	☒ Gas / Pressurised containers
Other/Details: Butane torch cylinder		
Environment		
☐ Sun exposure	☐ Water (creek, river, beach, dam)	☐ Sound / Noise
☐ Animals / Insects	☐ Storms / Weather	☐ Temperature (heat, cold)
Other/Details:		
Facilities / Built Environment		
☐ Buildings and fixtures	☐ Driveway / Paths	☐ Workshops / Work rooms
☐ Playground equipment	☐ Furniture	☐ Swimming pool
Other/Details: Lighting levels		
Machinery, Plant and Equipment		
☐ Machinery (fixed plant)	☐ Machinery (portable)	☒ Hand tools
☐ Vehicles / trailers		
Other/Details: Hot work		
Manual Tasks / Ergonomics		
☐ Manual tasks (repetitive, heavy)	☐ Working at heights	☐ Restricted space
Other/Details:		
People		
☐ Students	☐ Staff	☐ Parents / Others
☐ Physical	☐ Psychological / Stress	
Other/Details:		
Other Hazards / Details		

Step 2: Assess the Level of Risk

Consider the hazards identified in Step One and use the risk assessment matrix below as a guide to assess the risk level.

Likelihood	**Consequence**				
	Insignificant	Minor	Moderate	Major	Critical
Almost Certain	Medium	Medium	High	Extreme	Extreme
Likely	Low	Medium	High	High	Extreme
Possible	Low	Medium	High	High	High
Unlikely	Low	Low	Medium	Medium	High
Rare	Low	Low	Low	Low	Medium

Consequence	Description of Consequence
1. Insignificant	No treatment required
2. Minor	Minor injury requiring First Aid treatment (e.g. minor cuts, bruises, bumps)
3. Moderate	Injury requiring medical treatment or lost time
4. Major	Serious injury (injuries) requiring specialist medical treatment or hospitalisation
5. Critical	Loss of life, permanent disability or multiple serious injuries

Likelihood	Description of Likelihood
1. Rare	Will only occur in exceptional circumstances
2. Unlikely	Not likely to occur within the foreseeable future, or within the project lifecycle
3. Possible	May occur within the foreseeable future, or within the project lifecycle
4. Likely	Likely to occur within the foreseeable future, or within the project lifecycle
5. Almost Certain	Almost certain to occur within the foreseeable future or within the project lifecycle

Assessed Risk Level		Description of Risk Level	Actions
☐	Low	If an incident were to occur, there would be little likelihood that an injury would result.	Undertake the activity with the existing controls in place.
☐	Medium	If an incident were to occur, there would be some chance that an injury requiring First Aid would result.	Additional controls may be needed.
☐	High	If an incident were to occur, it would be likely that an injury requiring medical treatment would result.	Controls will need to be in place before the activity is undertaken.
☐	Extreme	If an incident were to occur, it would be likely that a permanent, debilitating injury or death would result.	Consider alternatives to doing the activity. Significant control measures will need to be implemented to ensure safety.

Step 3: Control the Risk

In the table below:

1. List below the hazards/risks you identified in Step One.
2. Rate their risk level (refer to information contained in Step Two to assist with this).
3. Detail the control measures you will implement to eliminate or minimise the risk.
   Note: Control measures should be implemented in accordance with the preferred **hierarchy of control**.

Hierarchy of Control	
Most effective (High level)	**Elimination**: remove the hazard completely from the workplace or activity
	Substitution: replace a hazard with a less dangerous one (e.g. a less hazardous chemical)
	Redesign: making a machine or work process safer (e.g. raise a bench to reduce bending)
	Isolation: separate people from the hazard (e.g. safety barrier)
	Administration: putting rules, signage or training in place to make a workplace safer (e.g. induction training, highlighting trip hazards)
Least effective (Low level)	**Personal Protective Equipment (PPE)**: Protective clothing and equipment (e.g. gloves, hats)

Activity *Step-by-step breakdown of the task*	**Hazards** *Hazards associated with each step*	**Inherent Risk** *Before control measures are put in place*	**Controls** *Measures that need to be taken to eliminate or minimise the risk associated with each hazard*	**Residual Risk** *After control measures have been put into place*
Set up workspace	Manual handling	C2L3	Wear gloves, two-person lift for any heavy objects	C2L2
	Trips, slips, and falls	C2L3	Wear safety boots, clear area around workbench	C2L2
	Knock equipment off workbench	C3L3	Wear safety boots with metatarsal protection	C1L2
Cut pipe and tees	Cuts and abrasions	C3L3	Use appropriate tools, deburr pipe ends, file edges of tees, wear gloves	C1L2
Drill holes in pipes	Workpiece moves, drill bit slips	C3L3	Use pipe vice, centre pop holes, use pilot drill, sharpen bits if needed	C1L2
	Cuts and abrasions	C2L2	File and deburr holes, wear gloves	C1L2
Solder socket to pipe	Chemical contact with flux	C1L3	Follow manufacturer's direction for use	C1L2
	Hot work	C3L3	Remove flammable materials from work area, light butane torch using sparker, have fire extinguisher ready to use, use a spotter to keep an eye out for sparks and smouldering	C2L2
	Burns	C3L3	Wear welding gloves, be mindful of hot surfaces	C1L2
	Fumes	C2L3	Ensure adequate ventilation	C1L2

Activity *Step-by-step breakdown of the task*	**Hazards** *Hazards associated with each step*	**Inherent Risk** *Before control measures are put in place*	**Controls** *Measures that need to be taken to eliminate or minimise the risk associated with each hazard*	**Residual Risk** *After control measures have been put into place*
Fix tees to pipe	Chemical contact with silicon	C1L3	Follow manufacturer's directions for use	C1L2

Risk Assessment Template

Use this template to document a risk assessment to manage health and safety hazards and risks.
For more details on the risk management process refer to, *Managing Health and Safety Risks*.

Note: For risk assessments with curriculum activities refer to: *Managing Risks in School Curriculum Activities*.

Activity Description: **Solder microphone and speaker**	
Conducted by: **David McLaughlin**	Date: **02 Sept 2014**

Step 1: Identify the Hazards

Biological (e.g. hygiene, disease, infection)		
☐ Blood / Bodily fluid	☐ Virus / Disease	☐ Food handling
Other/Details:		
Chemicals Note: Refer to the label and Safety Data Sheet (SDS) for the classification and management of all chemicals.		
☐ Non-hazardous chemical(s)	☐ 'Hazardous' chemical (Refer to a completed hazardous chemical risk assessment)	
Name of chemical(s) / Details:		
Critical Incident – resulting in:		
☐ Lockdown	☐ Evacuation	☐ Disruption
Other/Details:		
Energy Systems – incident / issues involving:		
☒ Electricity (incl. Mains and Solar)	☐ LPG Gas	☐ Gas / Pressurised containers
Other/Details: Soldering iron		
Environment		
☐ Sun exposure	☐ Water (creek, river, beach, dam)	☐ Sound / Noise
☐ Animals / Insects	☐ Storms / Weather	☐ Temperature (heat, cold)
Other/Details:		
Facilities / Built Environment		
☐ Buildings and fixtures	☐ Driveway / Paths	☐ Workshops / Work rooms
☐ Playground equipment	☐ Furniture	☐ Swimming pool
Other/Details: Lighting levels		
Machinery, Plant and Equipment		
☐ Machinery (fixed plant)	☐ Machinery (portable)	☒ Hand tools
☐ Vehicles / trailers		
Other/Details:		
Manual Tasks / Ergonomics		
☐ Manual tasks (repetitive, heavy)	☐ Working at heights	☐ Restricted space
Other/Details:		
People		
☐ Students	☐ Staff	☐ Parents / Others
☐ Physical	☐ Psychological / Stress	
Other/Details:		
Other Hazards / Details		

Step 2: Assess the Level of Risk

Consider the hazards identified in Step One and use the risk assessment matrix below as a guide to assess the risk level.

Likelihood	**Consequence**				
	Insignificant	Minor	Moderate	Major	Critical
Almost Certain	Medium	Medium	High	Extreme	Extreme
Likely	Low	Medium	High	High	Extreme
Possible	Low	Medium	High	High	High
Unlikely	Low	Low	Medium	Medium	High
Rare	Low	Low	Low	Low	Medium

Consequence	**Description of Consequence**
1. Insignificant	No treatment required
2. Minor	Minor injury requiring First Aid treatment (e.g. minor cuts, bruises, bumps)
3. Moderate	Injury requiring medical treatment or lost time
4. Major	Serious injury (injuries) requiring specialist medical treatment or hospitalisation
5. Critical	Loss of life, permanent disability or multiple serious injuries

Likelihood	**Description of Likelihood**
1. Rare	Will only occur in exceptional circumstances
2. Unlikely	Not likely to occur within the foreseeable future, or within the project lifecycle
3. Possible	May occur within the foreseeable future, or within the project lifecycle
4. Likely	Likely to occur within the foreseeable future, or within the project lifecycle
5. Almost Certain	Almost certain to occur within the foreseeable future or within the project lifecycle

Assessed Risk Level		**Description of Risk Level**	**Actions**
☐	Low	If an incident were to occur, there would be little likelihood that an injury would result.	Undertake the activity with the existing controls in place.
☐	Medium	If an incident were to occur, there would be some chance that an injury requiring First Aid would result.	Additional controls may be needed.
☐	High	If an incident were to occur, it would be likely that an injury requiring medical treatment would result.	Controls will need to be in place before the activity is undertaken.
☐	Extreme	If an incident were to occur, it would be likely that a permanent, debilitating injury or death would result.	Consider alternatives to doing the activity. Significant control measures will need to be implemented to ensure safety.

Step 3: Control the Risk

In the table below:

1. List below the hazards/risks you identified in Step One.
2. Rate their risk level (refer to information contained in Step Two to assist with this).
3. Detail the control measures you will implement to eliminate or minimise the risk.
   Note: Control measures should be implemented in accordance with the preferred **hierarchy of control**.

Hierarchy of Control	
Most effective (High level)	**Elimination**: remove the hazard completely from the workplace or activity
	Substitution: replace a hazard with a less dangerous one (e.g. a less hazardous chemical)
	Redesign: making a machine or work process safer (e.g. raise a bench to reduce bending)
	Isolation: separate people from the hazard (e.g. safety barrier)
	Administration: putting rules, signage or training in place to make a workplace safer (e.g. induction training, highlighting trip hazards)
Least effective (Low level)	**Personal Protective Equipment (PPE)**: Protective clothing and equipment (e.g. gloves, hats)

Activity *Step-by-step breakdown of the task*	**Hazards** *Hazards associated with each step*	**Inherent Risk** *Before control measures are put in place*	**Controls** *Measures that need to be taken to eliminate or minimise the risk associated with each hazard*	**Residual Risk** *After control measures have been put into place*
Set up workspace	Manual handling	C2L3	Wear gloves, two-person lift for any heavy objects	C2L2
	Trips, slips, and falls	C2L3	Wear safety boots, clear area around workbench	C2L2
	Knock equipment off workbench	C3L3	Wear safety boots with metatarsal protection	C1L2
Strip cables	Cuts and abrasions	C2L2	Use self-retracting knife, check sidecutters are in good condition	C1L2
Tin leads, solder leads to speaker and microphone	Electric shock	C4L2	Check condition of soldering iron supply cable and switches, use RCD	C3L1
	Burns	C2L3	Use damp sponge to clean tip, use jig to hold components in place, use holder tor soldering iron, turn off soldering iron and move it away when not in use	C2L2
	Cuts and abrasions	C1L2	Use sharp sidecutters to trim back ends of tinned leads	C1L2
	Fumes	C1L3	Use lead-free solder, ensure adequate ventilation	C1L1

Appendix C

Source Code

A selection of the most important MATLAB code listings are contained in this appendix. These include:

- `main`, the main script used to call other functions
- `fnSimChirpTrack`, the simulated waveform frequency tracking function
- `fnResChirpWin`, one of the functions used for windowing audio vectors from the resonator
- `fnResChirpTrack`, the initial resonator frequency tracking function
- `fnResTrackBand`, the improved resonator frequency tracking function
- `fnAudioRec`, a helper function for recording audio waveforms
- `fft_format`, a helper function for formatting FFTs
- `fnBufferFFT`, a wrapper function for processing FFTs used to reduce memory usage
- `fnMakeFilter`, a wrapper function for creating audio bandpass filters

```
% Main build script for ENG4111/4112 thesis
%
%         File:     main.m
%
%      Version:     2.72
%
% Last changed:     20141012
%
%      Purpose:
%
% Dependencies:
%
%      Outputs:
%
%       Author:     David McLaughlin

% Clear the variables and command window, and close any open figures
clc;
clear all;
close all;

% Set constants and flags
bPrint = 0;     % Flag to create PDFs of plots

% Initialise variables for this script
iFreq = 1600;   % Centre frequency for testing, Hertz
iFs = 44100;    % Sampling frequency in Hertz - 44.1kHz is CD quality
iDeltaF = 15;   % Change in frequency, Hertz/second

    % Prompt the user for the required waveform
    [theAction] = fnUserSelection(iFreq, iFs);

    switch theAction

        case '1'

            bNoise = 0;
            bReturn = fnSimSine(iFreq, iFs, bPrint, bNoise);

        case '2'

            bNoise = 1;
            bReturn = fnSimSine(iFreq, iFs, bPrint, bNoise);

        case '3'

            bReturn = fnSimChirpFFT(iFreq, iFs, bPrint, iDeltaF);

        case '4'

            bSegment = 1;
            bReturn = fnSimChirpTrack(iFreq, iFs, bPrint, iDeltaF, bSegment);

        case '5'

            bSegment = 1;
            bReturn = fnSimChirpWin(iFreq, iFs, bPrint, iDeltaF, bSegment);

        case '6'

            [bReturn, vFiltered] = fnResChirpTrack(iFs, bPrint, 1500, 1700);

        case '7'

            bReturn = fnResChirpWin(iFs, bPrint, 1575, 1625);

        otherwise

            bReturn = -1;

    end

    if bReturn ~=1
```

```
        fprintf('An error occurred during execution');

    end

% Clear the non-useful variables from the command window
clear bNoise bPrint bReturn theAction

% Bring the command window to the front
commandwindow;
```

```
function [ bReturn ] = fnSimChirpTrack( iFreq, iFs, bPrint, nDeltaFreq, bSegment )
%fnSimSine Simulate and plot sine wave at specified frequency, noise optional
%
%   Pass in required frequency, sample rate, and change in frequency.
%   Returns plots of the wave and frequency tracking of the wavefom.
%
    % Set constants for this function
    vBufferLength = floor(iFs/10);     % Size of window used for filter
    vBufferOverlap = floor(iFs/40);    % Overlap of window used for filter

    % Ensure sufficient waveforms for FFT
    iRepeats = 1600;

    % Total number of samples
    iSamples = ceil((iRepeats/iFreq) * iFs);

    % Time vector of samples
    vSample = (0:iSamples - 1) * (1/iFs);

    % nDeltaFreq is change in Hertz/second
    % Modify to change in Hertz over time 't'
    t1 = iRepeats/iFreq;
    f1 = round((t1 * nDeltaFreq) + iFreq);

    % Create sine chirp
    vSim = chirp(vSample, iFreq, t1, f1);

    % If bSegment is set, make a three-segment chirp
    if bSegment

        vSim = [vSim, sin(2 * pi * f1 * vSample)];
        vSim = [vSim, chirp(vSample, f1, t1, iFreq)];

    end

    % Set number of samples in FFT
    iLength = length(vSim);
    Nfft = ceil(iLength/iFs) * iFs;

    % Window and buffer the samples
    % Create the window
    vWin = hann(vBufferLength);
    % Split the samples into buffers with a small overlap
    mBuffer = buffer(vSim, vBufferLength, vBufferOverlap);
    % Remove zero padding at start and end of each frame
    mBuffer = mBuffer(:, 2:end-1);
    % Window each frame of the buffer
    mBuffer = (  mBuffer' * diag(vWin)  )';

    % FFT each frame
    mFFT = abs(fft(mBuffer, Nfft));
    mFFT = mFFT(1:length(mFFT)/2, :);
    % Find the frequency corresponding to the maximum FFT values
    [~, maxIndex] = max(mFFT);
    % Work out y-axis scaling
    maxIndex = maxIndex * iFs / Nfft;
    % Work out x-axis scaling in milliseconds
    xValues = (1:length(maxIndex)) * (vBufferLength/iFs - vBufferOverlap/iFs) * 1000;

    fprintf('There are a total of %2d points\n', length(maxIndex));
    fprintf('There are %3.0f milliseconds between sample points\n\n', xValues(1));

    % Plot the frequency tracking curve
    hFig = figure;
    sTitle = 'Chirp frequency tracking';
    plot(xValues, maxIndex, 'LineWidth', 2);
    plot_reduce(hFig, sTitle, 'Time (ms)', 'Frequency (Hz)', bPrint);
    set(gca, 'ylim', [min(maxIndex) max(maxIndex)+1]);

    bReturn = 1;

end
```

```matlab
function [ bReturn ] = fnResChirpWin( iFs, bPrint, loChirp, hiChirp )
%fnResChirpWin Record and plot audio signal of an ascending chirp
%
%   Pass in sample rate, high and low bandpass edges
%   Returns plots of the wave and frequency tracking of the wavefom
%   Essentially the same as fnResChirpTrack, but with rectangular window
%

    % Set constants for this function
    vBufferLength = floor(iFs/10);      % Size of window used for filter
    vBufferOverlap = 0;                 % Overlap of window used for filter

    % Record the audio sample
    [bRecorded, vRecording] = fnAudioRec(iFs);

    if bRecorded == 0

        % Audio wasn't recorded - don't continue
        fprintf('Exiting function - no audio to process\n\n');
        bReturn = 0;
        return

    end

    % Filter the audio
    theFilter = fnMakeFilter(iFs, loChirp - 10, loChirp, hiChirp, hiChirp + 10);
    vFiltered = filter(theFilter, 1, vRecording);

    % Window and buffer the samples
    % Create the window
    vWin = rectwin(vBufferLength);
    % Split the samples into buffers with a small overlap
    mBuffer = buffer(vFiltered, vBufferLength, vBufferOverlap);
    % Remove zero padding at start and end of each frame
    mBuffer = mBuffer(:, 2:end-1);
    % Window each frame of the buffer
    mBuffer = (  mBuffer' * diag(vWin)  )';

    clear vFiltered vRecording

    % Set number of samples in FFT
    iLength = size(mBuffer, 1);
    Nfft = ceil(iLength/iFs) * iFs;

    % FFT each frame
    mFFT = abs(fft(mBuffer, Nfft));
    mFFT = mFFT(1:length(mFFT)/2, :);
    % Find the frequency corresponding to the maximum FFT values
    [~, maxIndex] = max(mFFT);
    % Work out y-axis scaling
    maxIndex = maxIndex * iFs / Nfft;
    % Work out x-axis scaling in milliseconds
    xValues = (1:length(maxIndex)) * (vBufferLength/iFs - vBufferOverlap/iFs) * 1000;

    fprintf('There are a total of %2d points\n', length(maxIndex));
    fprintf('There are %3.0f milliseconds between sample points\n\n', xValues(1));

    % Plot the frequency tracking curve
    hFig = figure;
    sTitle = 'Chirp frequency tracking';
    plot(xValues, maxIndex, 'LineWidth', 2);
    plot_reduce(hFig, sTitle, 'Time (ms)', 'Frequency (Hz)', bPrint);
    set(gca, 'ylim', [min(maxIndex) max(maxIndex)+1]);

    bReturn = 1;

end
```

```
function [ bReturn, vFiltered ] = fnResChirpTrack( iFs, bPrint, loChirp, hiChirp )
%fnResChirpTrack Record and plot audio signal of an ascending chirp
%
%   Pass in sample rate, high and low bandpass edges
%   Returns plots of the wave and frequency tracking of the wavefom
%
    % Set constants for this function
    vBufferLength = floor(iFs/12);      % Size of window used for filter
    vBufferOverlap = floor(iFs/14);     % Overlap of window used for filter

    % Record the audio sample
    [bRecorded, vRecording] = fnAudioRec(iFs);

    if bRecorded == 0

        % Audio wasn't recorded - don't continue
        fprintf('Exiting function - no audio to process\n\n');
        bReturn = 0;
        return

    end

    % Filter the audio
    theFilter = fnMakeFilter(iFs, loChirp - 10, loChirp, hiChirp, hiChirp + 10);
    vFiltered = filter(theFilter, 1, vRecording);

    % Remove the first half second - microphone noise on initial switch-on
    vFiltered = vFiltered(iFs/2:end);

    % Window and buffer the samples
    % Create the window
    vWin = kaiser(vBufferLength, 2.5);
    % Split the samples into buffers with an overlap
    mBuffer = buffer(vFiltered, vBufferLength, vBufferOverlap);
    % Remove zero padding at start and end of each frame
    mBuffer = mBuffer(:, 2:end-1);
    % Window each frame of the buffer
    mBuffer = (  mBuffer' * diag(vWin)  )';

    % Set number of samples in FFT
    % Multiplier of 100/10/1 gives resolution of 0.01/0.1/1 Hz respectively
    iLength = size(mBuffer, 1);
    Nfft = ceil(iLength/iFs) * iFs * 10;

    iColumns = size(mBuffer, 2);
    maxIndex = zeros(1, iColumns);

    % Loop allows longer signals to be processed than is possible with vector math
    for iLoop = 1:iColumns

        maxIndex(1, iLoop) = fnBufferFFT(mBuffer(:, iLoop), Nfft);

    end

    % Work out y-axis scaling
    maxIndex = maxIndex * iFs / Nfft;
    % Work out x-axis scaling in milliseconds
    xValues = (1:length(maxIndex)) * (vBufferLength/iFs - vBufferOverlap/iFs) * 1000;

    fprintf('There are a total of %2d points\n', length(maxIndex));
    fprintf('There are %3.0f milliseconds between sample points\n\n', xValues(1));

    % Plot the frequency tracking curve
    hFig = figure;
    sTitle = 'Chirp frequency tracking';
    plot(xValues, maxIndex, 'LineWidth', 2);
    plot_reduce(hFig, sTitle, 'Time (ms)', 'Frequency (Hz)', bPrint);
    set(gca, 'ylim', [min(maxIndex) max(maxIndex)+1]);

    bReturn = 1;

end
```

```
function [ bReturn ] = fnResTrackBand( iFs, iStep, vFiltered )
%fnResTrackBand Plot frequency tracking curve for an audio vector
%
%   Pass in sample rate, required step size (ms), and audio vector
%   Returns peak frequency tracking plot
%

    % Calculate length of buffer windows given step size (ms) and sample frequency
    iWindowLength = floor(iFs * (iStep/1000));

    % Remove the first half second - microphone noise on initial switch-on
    vFiltered = vFiltered(iFs/2:end);

    % Split the audio samples into small chunks
    mBuffer = buffer(vFiltered, iWindowLength, 0);

    % Discard last frame - consistently ends up with too few samples
    mBuffer = mBuffer(:, 1:end-1);

    % Zero values at start and end of each frame
    for iLoop = 1:size(mBuffer, 2)

        x = diff(sign(mBuffer(:, iLoop)));
        theFirst = find(x>0, 1, 'first');
        theLast = find(x<0, 1, 'last');

        mBuffer(1:theFirst, iLoop) = 0;
        mBuffer(theLast:end, iLoop) = 0;

    end

    % Set number of samples in FFT
    % Multiplier of 100/10/1 gives resolution of 0.01/0.1/1 Hz respectively
    iLength = size(mBuffer, 1);
    Nfft = ceil(iLength/iFs) * iFs * 100;

    % FFT each frame
    mFFT = abs(fft(mBuffer, Nfft));
    mFFT = mFFT(1:length(mFFT)/2, :);

    % Find the frequency corresponding to the maximum FFT values
    [~, maxIndex] = max(mFFT);
    % Work out y-axis scaling
    maxIndex = maxIndex * iFs / Nfft;
    % Work out x-axis scaling in milliseconds
    xValues = (1:length(maxIndex)) * (iWindowLength/iFs) * 1000;

    fprintf('There are a total of %2d points\n', length(maxIndex));
    fprintf('There are %3.0f milliseconds between sample points\n\n', xValues(1));

    % Plot the frequency tracking curve
    hFig = figure;
    sTitle = 'Chirp frequency tracking';
    plot(xValues, maxIndex, 'LineWidth', 2);
    plot_reduce(hFig, sTitle, 'Time (ms)', 'Frequency (Hz)', 0);
    set(gca, 'ylim', [min(maxIndex) max(maxIndex)+1]);

    bReturn = 1;

end
```

```matlab
function [ bRecorded, vRecording ] = fnAudioRec( iFs )
%fnAudioRec Record signal at specified sample rate, return recorded vector
%
% The audio will block while recording
% There are also sanity checks for the recording time
% The recording is passed back from this function as a vector
%

    % Create audio recorder object
    % Assume 16 bit, 1 channel - change if necessary
    objAudio = audiorecorder(iFs, 16, 1);
    % Feedback to user when recording is occurring
    objAudio.StartFcn = 'disp(''Recording started'')';
    objAudio.StopFcn = 'disp(''Recording stopped'')';

    % Request recording time and process response
    theTime = input('Enter number of seconds to record: ');

    if (isempty(theTime) || ~isnumeric(theTime))

        theTime = 10;

    end

    if theTime < 0

        theTime = abs(theTime);

    end

    if theTime > 60

        theTime = 60;

    end

    % Prompt to start recording
    bStart = input(['\nReady to record ', int2str(theTime), ...
            ' seconds of audio? [Y/n] '], 's');

    if (isempty(bStart) || bStart == 'Y')

        % Record audio
        fprintf('\n');
        recordblocking(objAudio, theTime);
        vRecording=getaudiodata(objAudio);
        fprintf('\nRecording complete.\n');
        bRecorded = 1;

    else

        fprintf('\nRecording cancelled.\n\n');
        bRecorded = 0;

    end

end
```

```
function fft_format( hFigure, sName, sXlabel, sYlabel, bPrint, xFreq )
%FFT_FORMAT Format FFT plot to make it pretty
%   Set colours, fonts, labels, etc, for the FFT plots

    % Select the required figure
    figure(hFigure);

    % Set the name of the figure in the title bar
    set(gcf, 'Name', sName);

    % Make the axis colouring a little more unobtrusive
    set(gca, 'Xcolor', [0.5 0.5 0.5]);
    set(gca, 'Ycolor', [0.5 0.5 0.5]);

    % Set up the X axis ticks and labels
    set(gca, 'xlim', [0 xFreq]);
    set(gca, 'xtick', (0:xFreq/8:xFreq));
    xlabel(sXlabel, 'fontsize', 12, 'fontweight', 'b');

    % Y axis label
    ylabel(sYlabel, 'fontsize', 12, 'fontweight', 'b');

    % Set the grid on
    grid on;

    % Scale the plot to fit neatly on an A4 portrait sheet
    set(hFigure, 'Position', [50, 50, 891, 945])

    % Save as an EPS and print to PDF if bPrint is set
    if bPrint

        % Save the figure as an EPS file
        saveas(gcf, [sName, '.eps'], 'epsc');

        % Convert the EPS to a PDF for LaTeX
        system(['epstopdf ', sName, '.eps'])

    end

end
```

```
function [ maxIndex ] = fnBufferFFT( mBuffer, Nfft )
%fnBufferFFT Wrapper function for FFTs to reduce memory usage
%
    mFFT = fft(mBuffer, Nfft);
    mFFT = abs(mFFT);
    mFFT = mFFT(1:length(mFFT)/2, :);
    [~, maxIndex] = max(mFFT);

end
```

```
function [ theFilter ] = fnMakeFilter( iFs, iLowStart, iLowStop, iHighStart, iHighStop )
%fnMakeFilter Kaiser bandpass filter with specified sample rate and edges
%
% Pass in required sample rate and the edges of the band
% The filter is returned as the output of the function
%
% Filter the waveform using:
%   <filtered_vector> = filter(theFilter, 1, <raw_vector>)
%
    % These are the start and end of the slope for the band edges
    fcuts=[iLowStart iLowStop iHighStart iHighStop];

    % Magnitudes of the waveform inside and outside pass band
    mags = [0 1 0];

    % Maximum ripple inside and outside passband
    devs=[0.01 0.05 0.01];

    % Get the parameters for a Kaiser filter
    [n, Wn, beta, ftype] = kaiserord(fcuts, mags, devs, iFs);

    % Finally, the filter
    theFilter = fir1(n, Wn, ftype, kaiser(n+1, beta), 'noscale');

end
```

Appendix D

Manufacturer Data Sheets

Data sheets are included for the Jaycar ASS3030 speaker (Jaycar Electronics 2014*b*) and the Jaycar AM4008 microphone (Jaycar Electronics 2014*a*). The frequency response curve for the microphone was not legible in the supplied data sheet, and consequently another manufacturer data sheet which included the AM4008 microphone has also been included (Electus Distribution 2014).

CONTACT US

Free Call Order Line
- 1800 022 888

Email
- techstore@jaycar.com.au

Jaycar Stores

CAT. NO. AS3030

RRP	$8.95
QTY	
1+	$8.95
4+	$7.95
10+	$6.95

CLICK TO ENLARGE

CLICK TO ENLARGE

Shielded 1" 1W 8-Ohm Full Range Speaker

Full range speakers suitable for use in surround speakers in home theatre system, computer multimedia speakers and portable speaker designs. It has advanced alloy cone design coated with special damping material.

- 4 x screw mounting holes
- Dimensions: 36(L) x 36(W) x 13.1(D)mm

General Data
- Nominal Power Handling (Pnom)(W): 1
- Max Power Handling (Pmax)(W): 2
- Sensitivity (2.83v/1m)(dB): 79
- Weight (M)(Kg): 0.03

Electrical Data
- Nominal Impedance (Z)(Ω): 8
- DC (Re)(Ω): 6.5

Voice Coil and Magnet Parameters
- VC Diameter (mm): 19
- VC Length (H)(mm): 3.4
- VC Former: CCAW
- VC Frame: Kapton
- Magnet System: Shielded
- Magnet Former: Neodymium
- Force Factor (BL)(N/A): 2.3
- Gap Height (He)(mm): 1.5
- Linear Excursion (Xmax)(mm): 0.95

T-S Parameters
- Suspension Compliance (Cms)(uM/N): 626
- Mechanical Q (Qms): 3.9
- Electrical Q (Qes): 0.814
- Total Q (Qts): 0.674
- Moving Mass (Mms)(g): 0.56
- Effective Piston Area (Sd)(m2): 0.0005
- Equivalent Air Volume (Vas)(L): 0.04
- Resonance Frequency (Fs)(Hz): 270

AS3030_freq_curve.pdf

Enter Quantity 1

BUY NOW

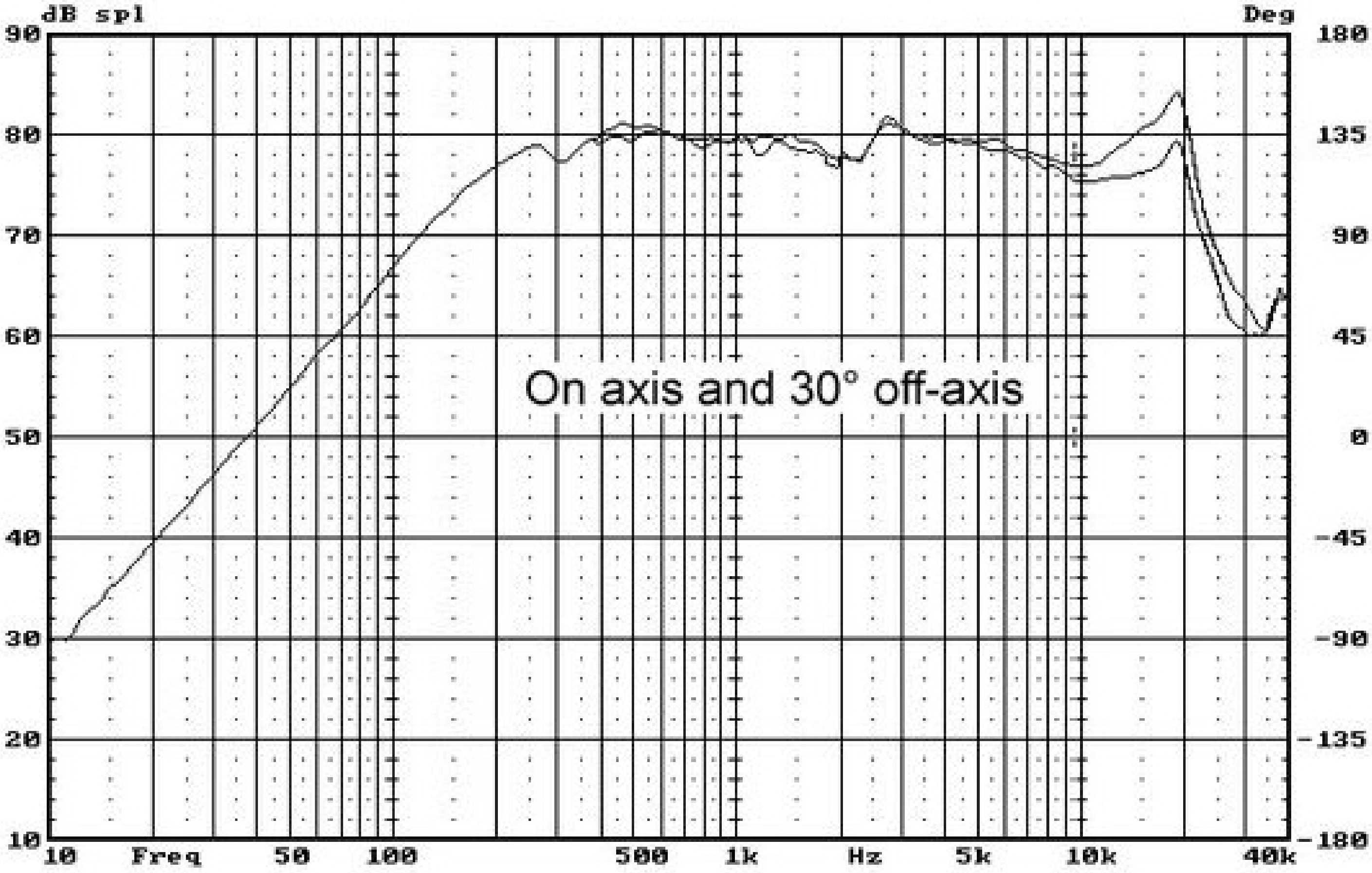

dB spl
Deg
90
80
70
60
50
40
30
20
10
180
135
90
45
0
-45
-90
-135
-180
10
Freq
50
100
500
1k
Hz
5k
10k
40k
On axis and 30° off-axis

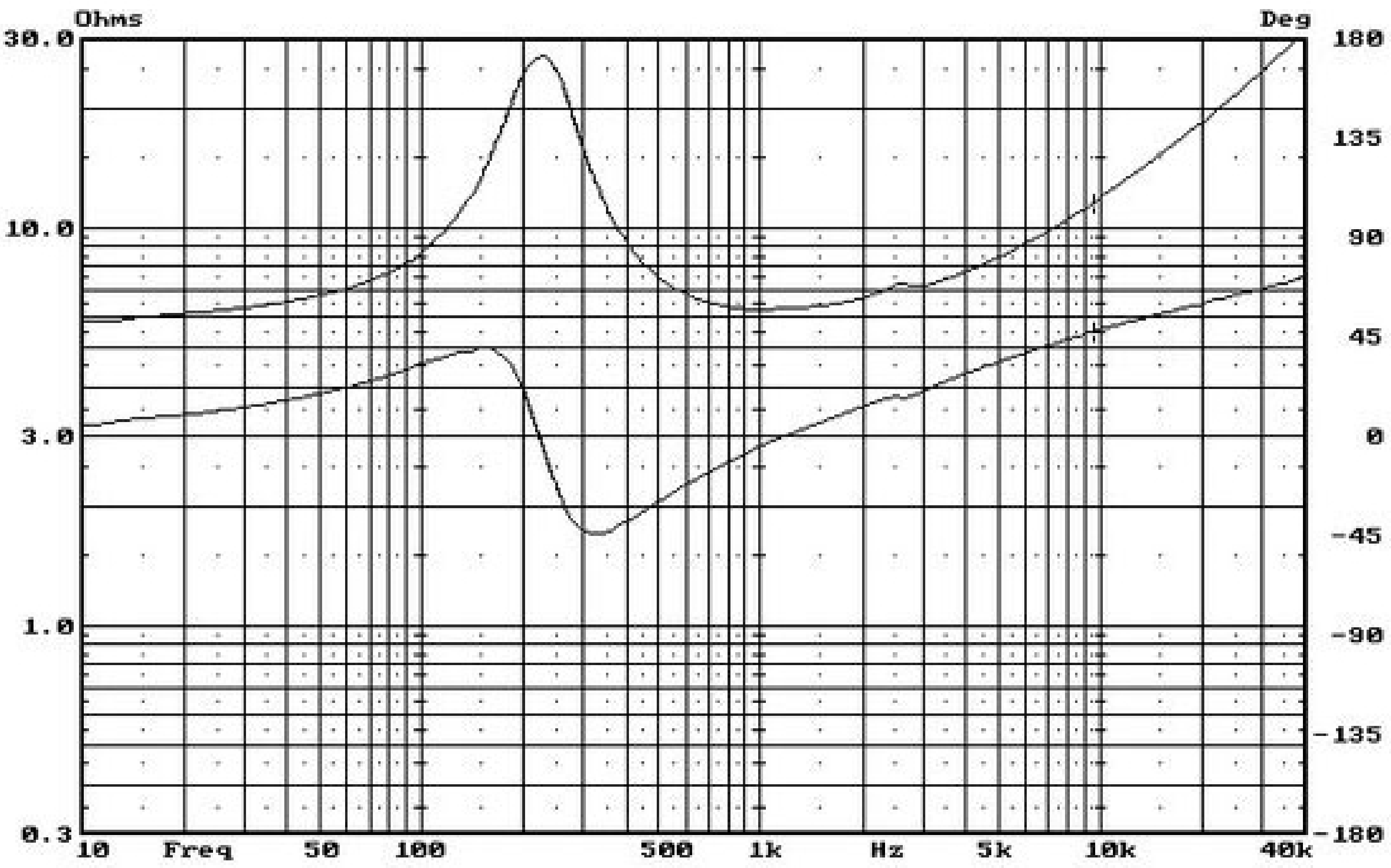

Ohms
Deg
30.0
10.0
3.0
1.0
0.3
180
135
90
45
0
-45
-90
-135
-180
10
Freq
50
100
500
1k
Hz
5k
10k
40k

CONTACT US

Free Call Order Line
- 1800 022 888

Email
- techstore@jaycar.com.au

Jaycar Stores

CAT. NO. AM4008

RRP $2.65

QTY	
1+	$2.65
4+	$2.30
10+	$2.07

CLICK TO ENLARGE

Mini Microphone Insert - 6 x 3.5mm

Omnidirectional mini mic insert. Ideal for all those miniature circuits.
Only 6mm diameter.

Specifications:
- Operating Voltage 1.5 to 15V DC
- Current Consump. 0.5mA or less (6V supply)
- Frequency Range 40 -10,000Hz
- Output Impedance Same as load resistance (150 ohm - 5k ohm)
- Sensitivity 66dB ±3dB
- S/N Ratio More than 40dB
- Size: 3.5mm x 6mm dia

This product is out of stock in our warehouse. Please check if your local store has stock.

AM4008.pdf

OUT OF STOCK

AM4008 - Electret Microphone Insert

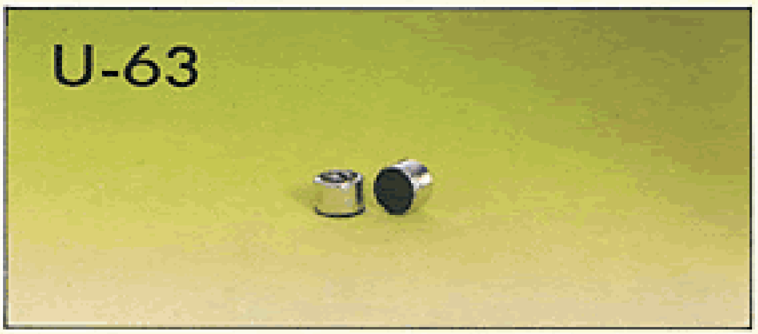

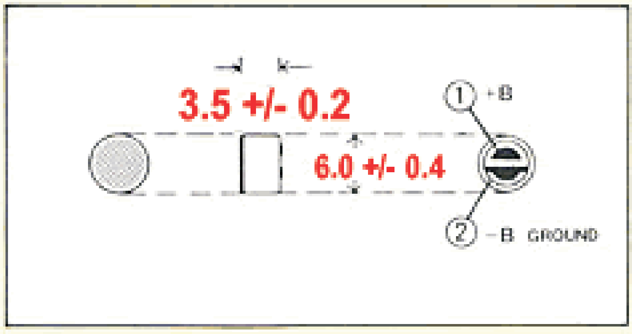

ELECTRICAL CHARACTERS	
1.SENSITIVITY 0dB = 1V/ μ bar at 1 KHz, RL = 1K Ω Vcc = 6V	A : -57 ± 3dB B : -63 ± 3dB C : -69 ± 3dB
2.OUTPUT IMPEDANCE	Same as the load resistance. (May be 150 Ω~5K Ω. The sensitivity is proportionate to the load resistance.)
3.DIRECTIONALITY	Omnidirectional.
4.FREQUENCY RANGE	50~12,500 Hz.
5.S/N RATIO	More than 40dB, Measured with A curve at 1Khz 1 μ bar.
6.SELF NOISE LEVEL	Less than 36dB SPL (Referred SPL 0dB = 0.0002 μ bar.)
7.OPERATION VOLTAGE	1.5 to 15 VDC.
8.CURRENT CONSUMPTION	0.8 mA or less (Supply voltage 6V)
9.POLARITY OF POWER SUPPLY	(–) for ground

10.FREQUENCY RESPONSE

U-63

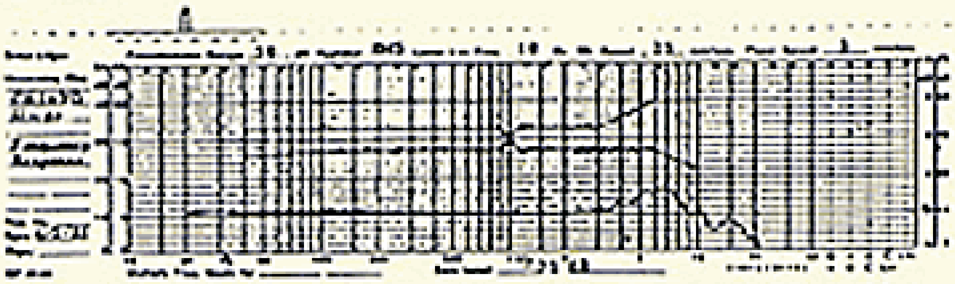

ELECTRICAL CIRCUIT

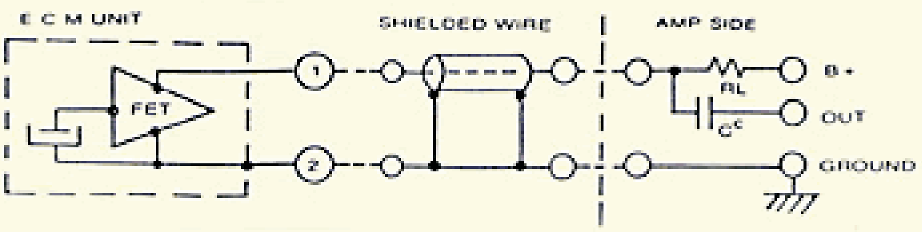

Distributied by Electus Distribution Pty. Ltd., Sydney. Ph. 1300 738 555

CHIAYO

ELECTRET CONDENSER MICROPHONE UNIT

MODEL NO. ACTUAL SIZE	DIMENSIONS SCALE:m/m

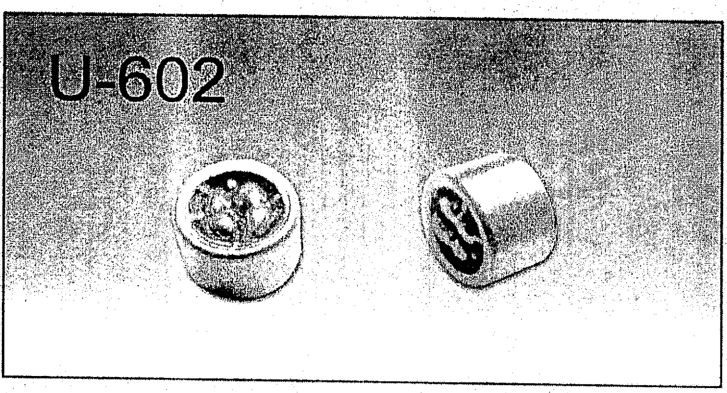

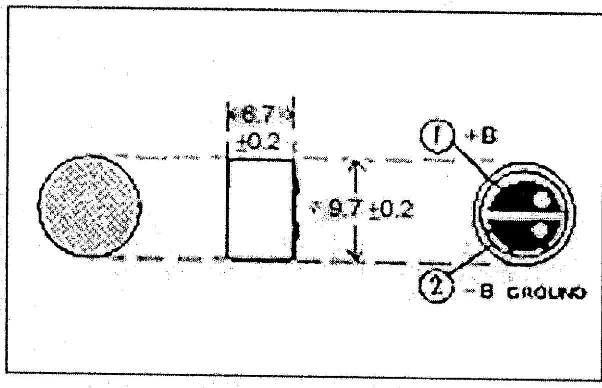

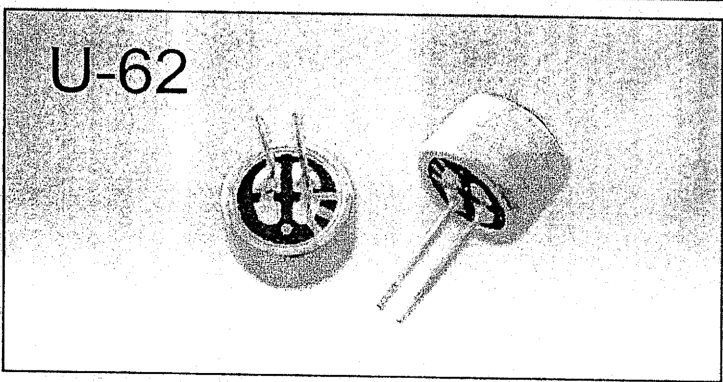

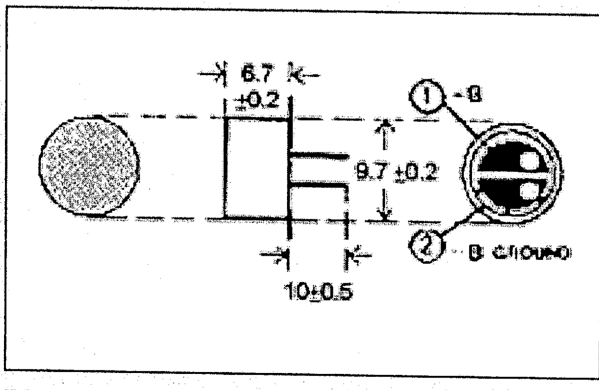

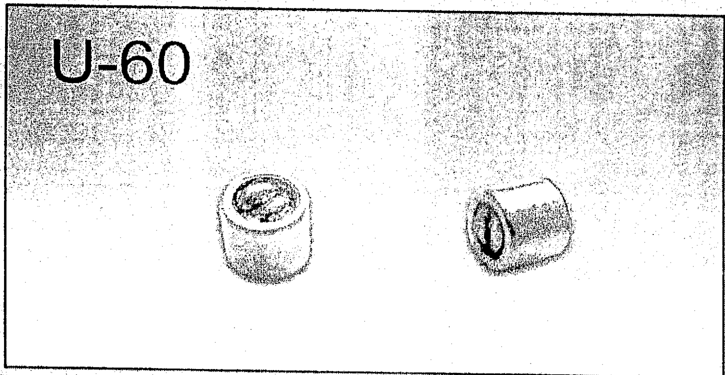

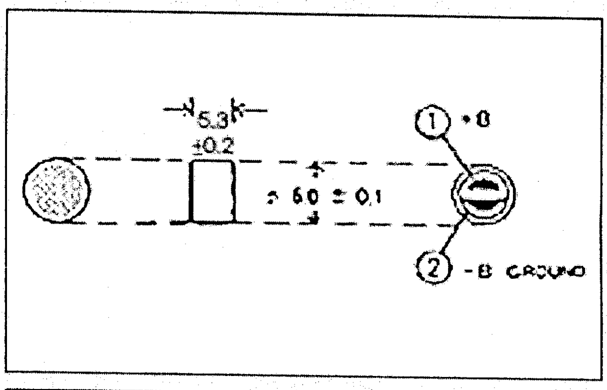

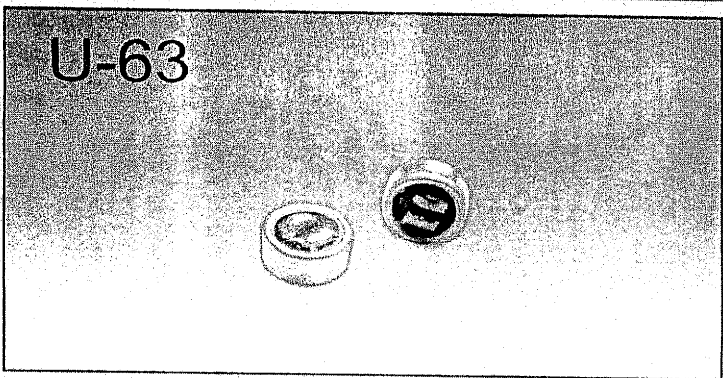

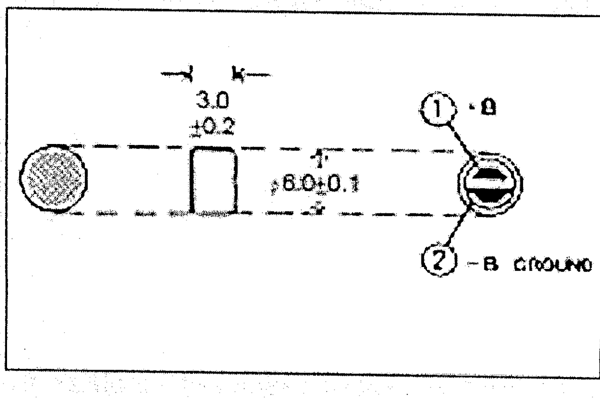

ELECTRICAL CHARACTERS	U-60	U-602	U-62	U-63
1.SENSITIVITY Vs=4.5v ,R1=2.2kΩ 0dB= 1V/ Ubar , 1 Khz	A: -58dB ±3dB B: -62dB ±3dB C: -68dB ±3dB	A: -58dB ±3dB B: -62dB ±3dB C: -68dB ±3dB		A: -58dB ±3dB C: -66dB ±3dB
2.OUTPUT IMPEDANCE	Less than 2.2kΩ			
3.DIRECTIONALITY	Ominidirectional			
4.FREQUENCY RANGE	20~16,000Hz			
5.S/N RATIO	More than 60dB			
6.OPERATION VOLTAGE	4.5V to 12V			
7.CURRENT CONSUMPTION	Max.0.5mA			

8.FREQUENCY RESPONSE

U-602

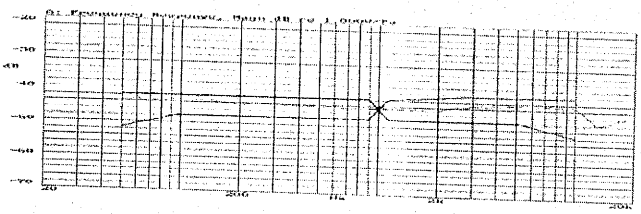

U-60

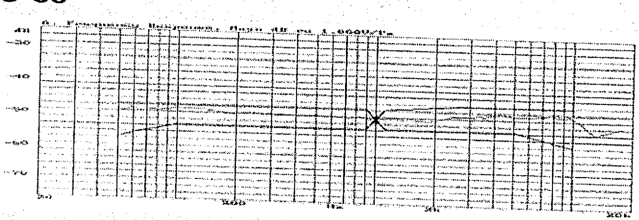

U-62

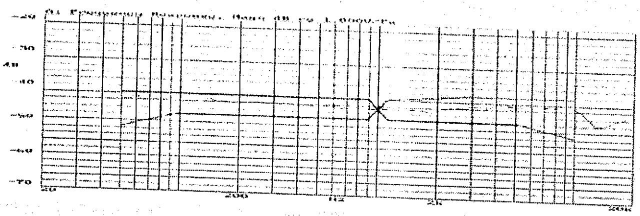

U-63

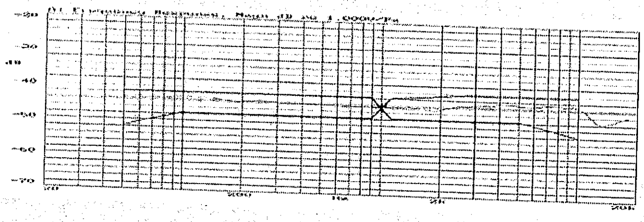

9.ELECTRICAL CIRCUIT

U-602

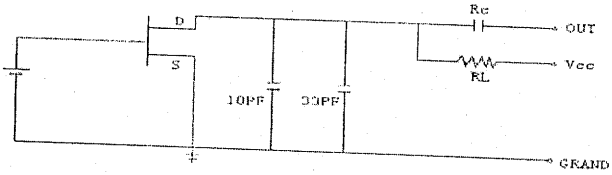

U-60

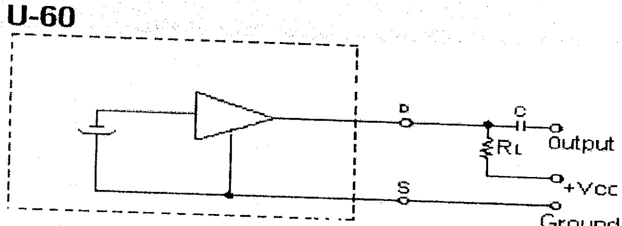

U-62

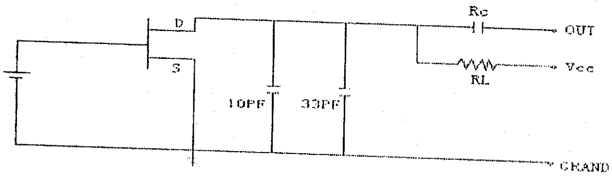

U-63

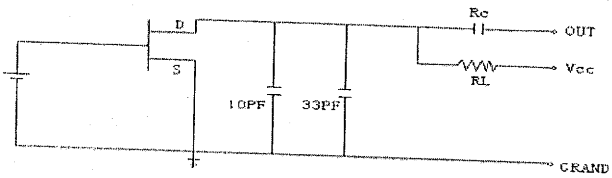

CHIAYO ELECTRONICS CO., LTD.

OFFICE: 30, L-27, S-4, Jen-Ai Rd., Taipei Taiwan. TEL:886-2-27415741 FAX:886-2-27525242
FACTORY: 88, Chung Hsiao Street.2, Chiayi Taiwan. TEL:886-5-2711000 FAX:886-5-2767611
http: //www.chiayo.com.tw E-mail: sales@chiayo.com.tw